EUROPEAN ORGANIZATION FOR NUCLEAR RESEARCH

CERN-EP/79-99
14 September 1979

INFLUENCE OF CHANNELLING ON SCATTERING OF 2-15 GeV/c PROTONS, π^+, AND π^- INCIDENT ON Si AND Ge CRYSTALS

S.K. Andersen, O. Fich, H. Nielsen, H.E. Schiøtt,

E. Uggerhøj and C. Vraast Thomsen

University of Aarhus, Denmark

G. Charpak, G. Petersen and F. Sauli

CERN, Geneva, Switzerland

J.P. Ponpon and P. Siffert

Centre de Recherches nucléaires (PHASE), Strasbourg, France

(Submitted to Nuclear Physics B)

Influence of Channeling on Scattering of 2-15-GeV/c Protons, π^+, and π^- Incident on Si and Ge Crystals

S.K. Andersen, O. Fich, H. Nielsen, H.E. Schiøtt,
E. Uggerhøj, and C. Vraast Thomsen
Institute of Physics, University of Aarhus
DK-8000 Aarhus C, Denmark
G. Charpak, G. Petersen, and F. Sauli
CERN, CH-1211 Geneva 23, Switzerland
J.P. Ponpon and P. Siffert
Centre de Recherches Nucléaires, PHASE
F-67037 Strasbourg-Cedex, France

Abstract

The channeling effect has a dramatic influence on scattering phenomena for GeV particles. Multiple scattering for positive particles is strongly reduced for incident directions close to the crystal axes and planes, resulting in a very high transmitivity along such directions, whereas negative particles experience increased multiple scattering along these directions. Correlated scattering from the atoms in atomic rows results in ring-shaped intensity distributions ("doughnuts") on the exit side which exist even for incident angles far beyond the critical angle for channeling. For such angles, we find a strongly increased multiple scattering for both positive and negative particles.

The yield from close-encounter processes such as wide-angle scattering and nuclear reactions is reduced to below 10% of normal yield for positive, channeled particles, whereas the yield is increased for negative particles. The measured dechanneling is found to be small even for a 4-mm thick Ge crystal. These results seem to agree fairly well with theoretical calculations based on a diffusion model. Computer calculations from a binary-collision model are in good agreement with experimental results. Also blocking effects are measured and agree fairly well with the dips obtained for close-encounter processes.

1. Introduction

The influence of crystalline structure on the penetration of high-energy particles is now being studied in various laboratories (Brookhaven[1], CERN[2-8], Dubna[9], Fermilab[10], LAMPF[11], Kharkov[12], Serphukov[9], and others).

A few years ago, there was a strong interest in extending the energy range (MeV/nucleon) of particles already used for channeling to the high-energy region. Here, strong relativistic effects are expected, and interesting opportunities are created by the new species of particles available for study, particularly the simultaneous observation of positive and negative particles of the same kind. As regards the ionization energy loss, the high-energy region was especially attractive since the theories of electronic energy loss of channeled particles gave distinctly different results in this region. Also, the use of strongly interacting particles of the same kind, differing only with respect to charge, as $\pi^+ - \pi^-$ was an interesting possibility. Here, large differences in the yield of nuclear reactions caused by positive and negative particles were expected.

Another strong motivation for the present study was the possibility of using channeling effects to measure ultra-short lifetimes of elementary particles[13]. Further, it would be interesting to measure the change in bremsstrahlung for channeled positive and negative particles. Attempts were made with MeV electrons and positrons, but technical problems made the experiments difficult and unattractive. In the high-energy region, where multiple scattering and dechanneling is low, many of these difficulties disappear[14]. A recent theory of Kumakhov[15] has further promoted the interest in measuring bremsstrahlung for channeled particles.

In the present paper, which is one in a series of reports from the Aarhus-CERN-Strasbourg collaboration, we wish to give a detailed analysis of the anomalous scattering phenomena observed when the incoming particles are close to axial or planar directions in the target. In two previous papers, our results of the influence of channeling on energy loss[6] and nuclear reactions[7] were reported.

2. Some Relevant Channeling Concepts

2.1 Continuum string and critical angles

Directional effects for non-relativistic, positive particles penetrating single crystals have been described theoretically by Lindhard[1]. In his theory, where the validity of a classical picture is established, of the motion a main concept is the axial row of atoms or the atomic string. When a particle enters a crystal at a small angle relative to the string, the correlation between successive collisions with atoms in the string causes the particle to be gently steered away from the string. Consequently, the yield of processes requiring small impact parameters is expected to be strongly reduced compared to what is the case in an amorphous substance. In a first approximation, the atomic string may be described by a continuum potential,

$$U(r) = \int_{-\infty}^{\infty} \frac{dz}{d} V(\sqrt{z^2+r^2}) \quad , \qquad (1)$$

where r is the distance from the string, $V(R)$ is the ion-atom potential, and d is the distance between atoms in the string. The quantity $U(r)$ plays the role of potential energy for the transverse motion of the particle, i.e., the motion

projected onto a plane perpendicular to the string direction. The continuum potential corresponding to motion along the <100> direction in copper is shown in fig. 2. For $V(R)$, a Thomas-Fermi-type potential with a screening length $a \simeq a_o \times Z_2^{1/3}$ was used, where a_o is the Bohr radius. The effective potential is seen to be rather flat in the region between strings and to rise steeply for distances around a ($\sim$0.15 Å), which are small compared to the distance between strings ($\sim$2-3 Å).

A qualitative condition for the continuum approximation is obtained by the requirement that the scattering in the vicinity of closest approach is due to many atoms. This sets an upper limit ψ_1 to the angle of incidence, for which there is a strong suppression of close collisions with string atoms. For incident angles smaller than ψ_1, the distance of closest approach is $\gtrsim a$.

At relativistic energies, it can be shown that the same picture applies provided the rest mass M_1 of the projectile is replaced by its relativistic mass (and hence the projectile energy $E = \frac{1}{2}M_1v^2$ by $\frac{1}{2}pv$, where p is the relativistic momentum of the projectile). The critical angle ψ_1 for axial channeling is[16)]

$$\psi_1 = \sqrt{4Z_1Z_2e^2/pvd} \quad . \tag{2}$$

The atomic planes have a similar steering effect. The critical angle for planar channeling ψ_p is found to be

$$\psi_p = \sqrt{4Z_1Z_2e^2Nd_pCa/pv} \quad , \tag{3}$$

where N is the atomic density of the target atoms, d_p is the distance between atomic planes, and C is a constant of the order of $\sqrt{3}$. In table 1, values of ψ_1 for the present experiment are given.

The application of a classical orbital picture is discussed in detail by Lindhard[16]. For a pure Coulomb potential and small scattering angles, Bohr[21] showed that a well-defined classical orbit can be expected if

$$\kappa = R_o/\lambda\!\!\!^{-} = 2Z_1Z_2e^2/\hbar v >> 1 \quad , \tag{4}$$

where R_o is the collision diameter and $\lambda\!\!\!^{-}$ is the de Broglie wavelength of the projectile. The Bohr condition may then be applied to the transverse plane, which means that

$$R_o \to a \quad (\text{for } \psi \sim \psi_1) \quad \text{and} \quad \lambda \to \lambda_\perp = h/p_\perp = h/p\psi_1 \quad .$$

Hence, according to the Bohr condition,

$$\kappa_\perp = a/\lambda\!\!\!^{-}_\perp = 2\left(\frac{\gamma M_1}{m_o} Z_2^{1/3} \times Z_1 \frac{a_o}{d}\right)^{\frac{1}{2}} > 1 \quad , \tag{5}$$

where $\gamma M_1/m_o$ is the ratio between the projectile mass and the electron rest mass. Clearly, $\kappa_\perp >> 1$ for all particles heavier than the electron. Further, $\kappa_\perp$ is increasing with increasing particle energy because of the appearance of the mass γM_1. For more details, the reader is referred to ref. 16.

2.2 Channeled and random beam

A particle having a transverse energy $\frac{1}{2}pv\theta_{in}^2$ outside the crystal (where θ_{in} is the incident angle to the atomic strings), upon entrance will achieve a transverse energy of

$$E = \tfrac{1}{2}pv\theta_{in}^2 + U(\vec{r}_{in}) \quad , \tag{6}$$

where $\vec{r}_{in}$ determines the point of entry in the transverse plane. As mentioned above, this transverse energy will in a first approximation be conserved. Particles with $E_\perp < \frac{1}{2}pv\psi_1^2$ belong to the channeled beam, for which close encounters with crystal atoms are strongly suppressed. The reduction in yield, for zero incident angle, of close-encounter processes (i.e., nuclear reactions, wide-angle scattering, inner-shell x-ray excitations, etc.) is found to be $\sim N \times d \times \pi\rho^2$, where ρ^2 is the average square amplitude of thermal vibrations and Nd is the number of strings per cm^2. This minimum yield is $\sim$1-2% of the random yield. Particles with $E_\perp > \frac{1}{2}pv\psi_1^2$ belong to the random beam, and for these particles close-encounter processes are possible. The motion of such particles may, however, still be influenced by the atomic rows, as was observed in transmission experiments with 5.5-MeV electrons in silicon[20]. In the high-energy region, we have even found that particles with transverse energies up to $\sim 100 \times \frac{1}{2}pv\psi_1^2$ experience some steering effect of the atomic strings, resulting in strong modifications of the multiple-scattering behaviour of the beam, as compared to random.

2.3 Dechanneling

The transverse energy $E_\perp$ of the channeled particle is not strictly conserved but may change due to scattering events. However, because positive particles are kept away from the atomic rows, normal multiple scattering is strongly suppressed although some scattering will occur caused by impurities and other crystal defects and, in particular, by electrons. The distribution in

transverse energy will therefore change gradually with depth, resulting in an increase of the average transverse energy. This process has been described as a diffusion in transverse energy. Gradually, channeled particles will be transferred to the random beam by this so-called dechanneling process.

2.4 Doughnuts

The flatness of the potential between the strings (cf. fig. 1) causes the distribution in transverse energy at zero depth to be strongly peaked around $\frac{1}{2}pv\theta_{in}^2$. String scattering will result only in rotations of the transverse-momentum vector $\bar{p}_\perp$. This means that in the transverse plane, the original direction of $\bar{p}_\perp$ will be changed, and after a certain number of string collisions, $\bar{p}_\perp$ may be in any direction in the transverse plane. This equalization process was discussed by Lindhard[15], who derived an approximate analytical formula, from which the crystal thickness necessary for such an equalization could be obtained. For thin crystals, where dechanneling is negligible, $E_\perp$ will not change appreciably in all of the crystal, and the particles will exit at angles to the crystal axis close to θ_{in} . Hence, the net result is that a parallel beam transmitted through the crystal will appear as a ring-shaped ("doughnut") distribution in angle space with a radius equal to θ_{in} . We have found doughnut patterns for incident angles considerably larger than ψ_1 .

2.5 Negative particles

For negative particles in general, no theory is available, but for heavy negative particles, for which a classical descrip-

tion is applicable, the description outlined above can be used. Thus, for collisions with atoms in the string, the negative particles "see" a potential opposite to that shown in fig. 1 with minima around the axis, and the collisions can be calculated as above. The result is that the negative particles are focused around the nuclei, causing an increase in close-encounter processes, multiple scattering, etc. The critical angle was expected to be proportional to ψ_1, which has also been demonstrated experimentally with ∿1-MeV electrons[17]. Dechanneling will be a much more serious problem for negative than for positive particles.

2.6 Monte-Carlo calculations

In order to further elucidate the motion of channeled particles, we have tried to simulate the penetration of relativistic particles through single crystals by computer calculations originally developed for electron- and positron-channeling studies[18], which follow the particle through a series of binary collisions with the crystal atoms. The two-body potential used is Lindhard's stardard potential[16], and the thermal vibrations of the crystal atoms are taken into account using a random number generator. The interaction with electrons in the crystal is neglected, and the lattice atom is assumed to be static during the collision. From the program are obtained distributions in scattering angles and impact parameters of a beam transmitted through a certain crystal thickness.

3. Experimental Setup

3.1 General layout

The experimental apparatus was installed in the P14 beam of the CERN 28-GeV/c Proton Synchrotron. A schematic layout of the experiment can be seen in fig. 2.

The beam was a high-intensity ($\sim 10^6$/cm^2/sec) secondary, non-separated, charged beam with a momentum adjustable between 2 and 15 GeV/c. Momentum slits allowed a reduction of intensity to limits acceptable for the detectors. In the positive polarity, the beam consisted of roughly equal amounts of protons and pions with about 2% of kaons, whereas in the negative polarity, it contained essentially only pions with 1% of antiprotons and kaons. The beam divergence was related to the momentum, as shown in table 2.

Particle identification was performed in two ways: For 2-GeV/c particles, the time-of-flight between SC1 and SC4, the two scintillation counters placed 16 m apart, was recorded. For the higher momenta, two threshold Cerenkov counters placed in front of SC1 were employed. The gas pressure in the Cerenkov counters was such chosen that a pion would give a signal in both counters, a kaon a signal in one and not in the other, and a proton no signal in any of them.

Two additional scintillation counters, SC2 and SC3, in anti-coincidence with SC1 and SC4, were used to define the usable fraction of the beam so as not to exceed the maximum size of the crystal sample at the focal point of the goniometer.

The incoming and outgoing particle trajectories were meas-

ured by a set of five position-sensitive drift chambers, DC1 through DC5. The beam lines VT1 and VT2 were evacuated to a pressure less than 10^{-2} torr, which essentially eliminates the contribution to multiple scattering from the air in the tube.

The goniometer allowed adjustment of the crystal axis to the average beam direction although a precise alignment was not necessary with this method. A suitable liquid-nitrogen cooling system could maintain the intrinsic detector at a nearly constant temperature of $\sim$90 K, and the pressure was kept below 10^{-6} torr.

3.2 Detection system

The basic principle of the experiment was to record both the incoming and outgoing angle to the crystal for each particle obeying the simple geometrical constraints already described, and at the same time to register the energy deposited in the crystal. Hence, we used a set of high-accuracy drift chambers to record, for each particle track, the coordinates (x,y) on the selected planes (DC1-DC5 in fig. 2). The active surface was 100×100 mm^2 for DC1-DC4 and 500×500 mm^2 for DC5. The latter was used for recording large scattering angles. The detailed behaviour of drift chambers has been described elsewhere[19].

The angular resolution of the detecting system is influenced by two factors: (i) The uncertainty in the coordinates from the drift chambers and the associated electronics of $\sim$0.1 mm, corresponding to a total angular uncertainty of $\sim$0.03 mrad. (ii) The uncertainty in the direction of the particle on entering and exiting the crystal caused by multiple scattering in the mylar windows and the airgaps close to the crystal. The second effect

is more serious at the lower energies and, in the actual setup, worse on the incident side than on the exit side. The multiple-scattering contribution was calculated in the same way as in ref. 4, i.e., based on the Bohr-Williams theory[21]. The calculated angular resolution (standard deviation) of incident and exit beams are tabulated in table 2. These values are in good accord with measurements performed on the system without the crystal.

In principle, the data acquisition was carried out as described in ref. 4. In short, for each accepted event, the output from the drift chambers, the crystal detector, and the Cerenkov counters, viz., the TOF measurement, was stored on magnetic tape. The CDC 7600 at CERN was used for the full data analysis, whereas a small on-line computer ensured correct behaviour of the detecting system.

3.3 Preparation of crystal detectors

Few elements form crystals suited for channeling experiments because the critical angles are that small that even a moderate mosaic spread will smear the channeling effects. In all experiments, we have used silicon and germanium crystals, which can be produced with a very low mosaic spread. These elements are well suited for the production of solid-state ionization detectors too, as discussed below.

A slight bending of the crystal will also lead to a smearing of the effects, and to avoid this, special crystal holders were constructed where the crystals were fixed without any stress being applied. The crystals were tested at room tempera-

ture with a double-crystal x-ray spectrometer. From the rocking curve, a very accurate measurement of the bending was obtained. Also x-ray topography was employed. Thus it was ensured that the crystals were bent no more than 10^{-2} mrad.

During the experiment, a final test on the crystal bending by means of the transmission effect was made. It should be noted that without the above precautions, it was not uncommon that the mounted samples were bent by as much as 5 mrad.

In order to use the crystals as pulse-height detectors, they were prepared in the following way: Germanium crystals were treated as reported in ref. 4. In short, high-purity N-type material was used with a net impurity concentration below $2.5\times10^{10}/cm^3$. Samples of various thicknesses ranging from 0.3 to 4.2 mm, with the <110> axis perpendicular to the surface, were prepared. Low-energy boron implantation was applied with no further annealing to produce the front rectifying contact, and a 200-Å aluminium layer was deposited as a back contact. Without any heating of the sample, this procedure ensured that the bulk of the material maintains its quality. Cooling of the samples was necessary only during measurements.

Silicon crystals were made of N-type material with resistivity in the range from 10 000 to 30 000 Ωcm. Samples of thicknesses between 0.3 and 1 mm and with the <100> or the <111> axis perpendicular to the surface were prepared. The front contact was made by implanting $10^{14}/cm^2$ 5-keV boron ions, followed by a 3-min anneal at 200°C to remove the radiation damage. The same backcontact as that for the germanium crystal was used.

Thus, the crystals, in which channeling conditions are established during the experiment, also serve as solid-state ionization detectors. When suitable bias voltage is applied to these crystals, an output pulse will be obtained from the associated electronics, which is precisely proportional to the energy deposit in the crystal by ionization processes. The system is energy-calibrated by irradiating the crystals with radioactive cobalt and barium sources. In most cases, the detectors were fully depleted during experiments, but the effective sensitive thickness could be varied by changing the bias.

3.4 Crystal alignment

As mentioned above, the incident beam is not parallel, and it suffices to align the crystal axis within the cone of incoming angles. In a previous experiment, the transmission patterns (see below) were utilized to establish the direction of the crystal planes. For each setting of the goniometer, a magnetic tape was filled and analyzed, and corrections in the crystal setting were made. The process was repeated until perfect alignment was obtained. This was a rather time-consuming process, especially since the crystal axis could be off the incident-beam cone by as much as a couple of degrees.

In the present case, the alignment was performed in a different and much faster way. We utilized the fact that positive particles experience lower-than-random energy loss when channeled along planes or axes. The pulse-height spectra from the crystal for all particles were fed into a multichannel analyzer. Such a spectrum is shown in fig. 3 and shows a situation where

the alignment is already perfect. The low-energy-loss group corresponds to the channeled particles. In a first setting of the crystal, only a small part of the beam particles happens to be aligned to some crystal planes, and the low-energy part of the spectrum is only a weak tail.

Electronically, two windows are set, one (W1) covering the low-energy-loss tail, the other (W2) covering the rest of the spectrum and used for normalization. When the relative number n of particles in W1 is plotted against the crystal tilt angle, a peak is recorded each time a plane or an axis is aligned to the beam. In this way, planes and axis are found very quickly without any use of a computer and with a goniometer with a minimum step size of $\sim$0.2 mrad.

Figure 4 shows an example of the alignment procedure for the 0.9-mm <110> silicon crystal, using 15-GeV/c π^+ as a beam. In the present case, the counts n in W1 are plotted for 10^4 events in W2. For the alignment were used two x scans and one y scan, followed by a final check to see if the setting of the axis does indeed give a maximum in n. The actual alignment lasted only two hours. Afterwards, some 2-300 000 events are stored on magnetic tape and analyzed to give a stereogram, showing the positions of axis and planes in the beam. For data reduction and normalization, see ref. 3.

4. Results and Discussions

4.1 Transmission experiments

For GeV particles transmitted through crystalline targets, the influence of channeling on the angular distribution behind

the target can be very dramatic. In fig. 5 is shown scans through the intensity distributions of 2- and 15-GeV/c protons transmitted through 0.3- and 4.2-mm thick germanium targets with the <110> axis inside the beam cone. The transmitted intensity along this axis is rather high compared to the intensity at angles larger than the critical angle for channeling ψ_1 . It is seen that the peak-to-background ratio varies going from fig 5a to 5c because the random multiple scattering in the three cases increases as follows: fig. 5a: 0.15 mrad; fig. 5b: 0.5 mrad; fig. 5c: 4.6 mrad, whereas the angular width of the transmission peak in all cases is about the same as the acceptance angle for channeling, viz., ψ_1 . A rather small reduction in peak intensity even for the thick crystals is found, showing that dechanneling is small. Thus a crystal aligned within a beam cone produces a beam with an angular spread of approx. ψ_1 , the critical channeling angle, and with a small reduction in intensity along the axial and planar directions.

In the early stages of our high-energy channeling experiments, it became evident that the most sensitive way to detect the channeling effect would be via transmission experiments in crystals thick enough that the r.m.s. random multiple-scattering angle $\vartheta_G >> \psi_1$. The crystal should not be that thick, however, that dechanneling substantially destroys the channeling effect, which is in good agreement with fig. 5, where fig. 5a shows that $\vartheta_G \sim \psi_1$ (small effect) while in figs. 5b and c $\vartheta_G >> \psi_1$ (very pronounced effect).

The background can be even further reduced by introducing

a small-angle-scattering criterion into the analysis. In figs. 6 and 7 is shown the intensity distribution in the incident-angle space of 15-GeV/c protons and π^- transmitted through a 4.2-mm <110> germanium crystal with a total scattering angle less than $\approx\frac{1}{2}\psi_1$. In both cases, a peak around the <110> axis is found, but the proton peak is much more pronounced and narrower than the π^- peak. The peaks are surrounded by an intensity dip, which for π^- is very broad. The random values are emerging at the edges of the plot. For negative particles, no planar effects have been obtained so far.

To get a more detailed picture of the intensity variations around the axial direction, circular integration with its center in the <110> axis was made. In fig. 8 is shown such circular integrations of 2-, 6-, and 15-GeV/c protons transmitted through 0.3-, 0.7-, and 4.2-mm germanium and 0.9-mm silicon crystals. The 0.9-mm silicon crystal will give the same random multiple scattering as did 0.4-mm germanium. For a certain incident direction (relative to the <110> axis), the plots show the fraction of particles (in percent) transmitted through the crystal with a scattering angle smaller than the cut angle α . Figures 8a-d show the effect of increasing the crystal thickness. It is seen that for germanium, the peak is independent of the actual thickness variation (practically no dechanneling), whereas the background is continuously being reduced. For random directions, the reduction can be evaluated as follows: With each incident direction is associated an approximately Gaussian distribution of angular width θ_G . Hence a small-angle-scattering criterion α

on the analysis will reduce the transmitted intensity by $\sim\alpha^2/\vartheta_G^2$. The intensity reduction for particles incident nearly paralled to the axis ($\psi \sim 0$) is very small for moderate crystal thicknesses (little dechanneling). The reason for the 60% reduction in figs. 8a-c is rather poor angular resolution in the detecting system (see table 2). With infinitely good angular resolution, the reduction in transmission should be negligible for an incident angle smaller than the channeling angle. The effect of varying the angle α can be seen from figs. 8b, e and f. In our experiment, the angular resolution for 15-GeV/c protons is $\sim\frac{1}{3}\psi_1$; hence angles α smaller than that are not well justified. The overall reduction of the random background is in agreement with the α^2/ϑ_G^2 ratio. The peak intensity reaches 75% in fig. 8e, where α is twice the angular resolution. As the random multiple scattering ϑ_G^2 is proportional to t/p^2 , where t is the crystal thickness and p the relativistic momentum, the most pronounced transmission effect should be seen for 2 GeV/c and the 4.2-mm thick crystal, but in that case, the influence of the detector resolution is greater than in the 15-GeV/c case, where the peak-to-background ratio is $\sim$15 (cf. table 2).

However, the angular width at half maximum of the peak is not really the quantity to be compared with ψ_1 because dechanneling is much more serious for the large-transverse-energy particles, and the width will mostly be determined by α , detector resolution, and multiple scattering of the channeled beam. It would be more appropriate to compare ψ_1 with the width at the base. From fig. 5 is seen that the proportionality between the

base and ψ_1 is rather good, but we shall refrain from a detailed analysis of this aspect of the data because the wide-angle-scattering results are much more accessible to a comparison with theoretical calculations.

In fig. 9 is shown the same type of circular integration for 15-GeV/c π^- incident on a 0.3-mm (a) and a 4.2-mm (b) <110> germanium crystal. In both cases, the cut angle is $\frac{1}{2}\psi_1$. It is seen that due to increased multiple scattering, the central peak for negative particles is slightly lower than the random value, with a pronounced minimum at about $2\psi_1$. Also, the width of the dip is much broader ($\sim 8\psi_1$). Such effects were already detected for MeV electrons and positrons[20]. The reason for the dip surrounding the central peaks for both positive and negative particles will be discussed in sec. 4.3.

In fig. 6 it was seen that for positive particles, the crystal planes have a similar steering effect as the axis has. Figure 10 shows that the {111} crystal plane can distort the transmitted intensity distribution of 15-GeV/c protons traversing the 4.2-mm germanium crystal. The scan across the beam is rather broad (1.5 mrad) but cuts through the side of the beam. The planar effect is clearly seen; there is even an increase in intensity on the planar side of the cut due to equalization of the variations in intensity distribution. In fig. 11 are shown cuts through the intensity distributions around the {111} and {112} planes for 15-GeV/c protons traversing the 4.2-mm germanium crystal. The cut angle was 0.05 mrad, i.e., slightly smaller than the overall angular resolution of 0.06 mrad, but still very pronounced peaks

are obtained with angular widths at the base comparable to the planar critical angle ψ_p which, for the {111} plane is 0.06 mrad. These extremely narrow but still very pronounced peaks make it possible to determine the axis position with the utmost accuracy, i.e., to within ∿0.01 mrad, thereby checking instabilities in alignment during the runs.

4.2 Multiple scattering

As mentioned above, the multiple scattering is expected to be strongly influenced by channeling, being mainly due to nuclear collisions which are strongly decreased for positive, channeled particles but increased for negative ones. In fig. 12 are plotted multiple-scattering distributions for 15-GeV/c protons and π^- traversing the 4.2-mm germanium crystal. The plots denoted 'random' correspond to a situation where the incident beam is far from the axis and planes; these results should therefore be equal to results obtained from an amorphous target. The random multiple scattering has been treated by several authors. A rather simple theory has been given by Bohr and Williams[21], who divide the distribution into a Gaussian part, resulting from small-angle multiple scattering, and a tail, mainly due to single-scattering events. The dashed curves in fig. 12 are Gaussian distributions

$$P(\vartheta)\,d(\vartheta^2/\vartheta_G^2) = ce^{-\vartheta^2/\vartheta_G^2}d(\vartheta^2/\vartheta_G^2) \qquad (7)$$

fitted to the data with $\vartheta_G = 0.5$ mrad. The expected theoretical value of ϑ_G due to multiple scattering in the target is determined from the equation

$$\vartheta_G^2 = 8\pi(Z_1Z_2e^2/pv)^2\,NR\log(pa\vartheta_G/\hbar) \qquad (8)$$

to be $\vartheta_G = 0.53$ mrad. Here Z_1 and Z_2 are the atomic numbers of projectile and target, respectively, p and v are the momentum and velocity, N is the density of the target atoms, a is the Thomas-Fermi screening length, and R is the crystal thickness. This formula reflects the idea that the mean-square scattering angle ϑ_G^2 of the Gaussian part is determined by scattering through angles smaller than ϑ_G. In the present case, the overall angular resolution of incident- and exit-angle determination of the tracks is small (0.06 mrad) compared to ϑ_G. The agreement between theory and experiment is seen to be good. By utilizing the Moliere theory[21] (solid curves), good agreement in the plural-scattering region is found too. For the well-aligned protons (fig. 12a), multiple scattering is seen to be considerably reduced. Here the ϑ_G value is only $\sim$0.15 mrad, corresponding to a reduction compared to random by a factor of 3.5, whereas well-aligned π^- shows a small increase (20%) in ϑ_G compared to random because some negative particles are bound to move close to the high-density nuclear region.

From the figure it is also seen that for both positive and negative particles, an angular region exists where the scattering is drastically increased. The distribution is no more Gaussian and the width is increased by 50-100%. This is caused by the doughnuts (see below), corresponding to a very broad region of incident angles.

In fig. 13 is plotted the variation in multiple scattering for 15-GeV/c protons and π^- traversing the 0.3-mm and the 4.2-mm germanium crystal. As a measure of the distributions, the

angular width $\vartheta_{1/e}$ is taken at the position where the intensity has decreased to e^{-1} of the maximum even for those distributions that are not Gaussian. The value $\vartheta_{1/e}$ is plotted as a function of the angle between incident-beam directions and the <110> axis in units of the critical angle $\psi_1 = 0.18$ mrad.

For positive particles, the multiple scattering is strongly reduced for incident angles up to $\sim\psi_1$ but increased by 10-20% for negative particles. The region where both positive and negative particles experience strongly increased scattering is seen to stretch out very far. Even for incident angles of $\sim 10\psi_1 \sim 2$ mrad, none of the particles exhibit normal multiple scattering. Since measurement of multiple-scattering distributions plays a dominant role in many high-energy experiments (e.g., calibration experiments), great care must be taken to ensure that the targets are not crystalline or polycrystalline with axial directions in the vicinity of the incident-beam cone.

4.3 Doughnuts

To get more insight in the fate of the angular distributions of narrow beams incident on a crystal, three-dimensional scatter plots of the intensity distributions in exit-angle space were made. Figure 14 shows such scatter plots for 15-GeV/c protons and π^- transmitted through a 0.3-mm thick <110> germanium crystal. The transmitted intensity is plotted as a function of the angle between the <110> axis and the exit direction. The incident-beam direction is indicated in the plots. The incident beam had an azimuthal spread of 30° and a radial spread of $\sim$0.1 mrad. Both distributions show that the correlated scattering from the atomic

strings results in a doughnut distribution centered around the <110> axis, with pronounced minima along the axial direction. A strong scattering in the azimuthal direction can also be observed, whereas the radial distribution experiences only little multiple scattering.

For a more detailed investigation of the phenomena, two scans through the distributions were made. In fig. 15 are shown such scans for 15-GeV/c protons (left-hand side) and π^- (right-hand side) traversing the 0.7-mm <110> germanium crystal (scanning directions shown at the top of the figure). In each figure, the incident beam is indicated as a square box with error bars indicating the angular resolution of the detecting system. The first four plots (1-4) correspond to incident angles up to ψ_1 . Here the protons yield a minimum and the π^- a maximum along the axis, showing that the diffusion in transverse energy for well-aligned particles is much stronger for negative than for positive particles. The intensity is nearly independent of azimuthal angle, showing a complete equalization in transverse momentum $\vec{p}_\perp$. Plots 5-7 correspond to incident angles between ψ_1 and $2\psi_1$. Here, both protons and π^- show a minimum along the axis, and for π^- , there is still eqialization in transverse momentum but not for protons. Plots 8-12 correspond to incident angles $2\psi_1$ to $3.3\psi_1$. Equalization in transverse energy has not been established for this crystal thickness (0.3 mm). The general result is that the tendency towards equilibrium is stronger for negative than for positive particles, indicating that the negative potential gives somewhat stronger scattering than the positive potential.

Similar doughnut patterns were already observed for MeV protons[22], positrons, and electrons[20] transmitted through thin crystals with incident angles to the axis up to $\sim\psi_1$, and the theory was developed by Golovchenko[23]. The most striking feature of the above doughnuts is that they appear for incident angles larger than ψ_1. This interesting characteristic is investigated further in fig. 16, where the ratio between the doughnut intensity at 180° (in azimuth) from the beam and that at the beam position is plotted. The curves are shown as a function of angle between incident direction and crystal axis. The results are shown for 6- and 15-GeV/c protons and π^- traversing 0.3-mm, 0.7-mm, and 4.2-mm crystals. In general, it is seen that high transverse energies require many string collisions to randomize the transverse momentum. Again, the curves show that the negative potential is somewhat more effective in doughnut formation than the positive potential.

Apparently the critical angle ψ_1 is not the limiting angle for doughnut formation. On the other hand, ψ_1 was calculated as the most restrictive condition for the application of the continuum description, i.e., only close-encounter processes, for which the impact parameter b is equal to zero, were considered. In fact, correlated scattering from many atoms in the axis is still present for incident angles larger than ψ_1, especially in the high-energy region where channeling angles are small. Taking into account the effective thermal amplitude ρ perpendicular to the atomic strings, it is easily seen that a quantitative condition for the continuum approximation is simply

$\rho > d\psi$, where ψ is the incident angle to the axis and d is the interatomic spacing in the string [24]. This condition on ψ corresponds to incident angles of $\lesssim 50$ mrad in germanium. Hence, for the analysis of the doughnuts, the continuum description is valid for the present experiment.

The problem of calculating the crystal thickness $\lambda_\perp$ needed to randomize the incoming transverse momentum $\vec{p}_\perp$ has been approached in two ways: (i) by analytical calculations, and (ii) by computer simulation of the binary collisions between projectile and the atoms in the string. Both methods are based on the simple classical picture of channeling given by Lindhard [16]. By using a simple approximation for the static string potential ($U(r) \sim 1/r$), Lindhard finds

$$\lambda_\perp = \frac{4\psi}{\pi^2 N d a \psi_1^2} \quad , \tag{9}$$

where ψ is the incident angle to the axis. The expression for $\lambda_\perp$ is rather sensitive to the potential approximation used, but the above formula is in reasonably good agreement with experiment for $\psi < \psi_1$. For the case of 15-GeV/c protons incident on <110> germanium, with $\psi = \psi_1$, one finds from Eq. (9) $\lambda_\perp \simeq 10\mu$. For $\psi > \psi_1$, a simple expression for $\lambda_\perp$ can be obtained by disregarding close collisions ($b < \rho$) and use a $1/r$ approximation for $U(r)$, which corresponds approximately to using a thermally averaged $1/r$ potential. This introduces a change in the Lindhard formula,

$$\lambda_\perp \simeq \frac{4\psi}{\pi^2 N d a \psi_1^2}[(\psi/\psi_1)^2 \ \rho/a] \quad , \quad \psi > \psi_1 \tag{10}$$

Here, ρ/a is of the order of ½-1. In general, the agreement between our experiments and the analytical expressions is good for incident angles $\psi \lesssim \psi_1$ but only fair for angles $\psi > \psi_1$, where the above formula gives $\lambda_\perp$ somewhat low. As is well known, the $1/r$ potential gives, for fixed impact parameters, the same scattering angle for positive and negative particles. More realistic potentials should be used to explain the different values of $\lambda_\perp$ observed experimentally.

Using Lindhard's standard potential for a static string, one finds, for $\psi \lesssim \psi_1$, $\lambda_\perp$ values of the same order of magnitude as given by Eq. (9), although for negative particles, $\lambda_\perp$ is somewhat larger than for positive particles, in agreement with computer calculations, to be discussed in section 4.4. Since our thinnest crystal was 0.3 mm thick, we have no experimental evidence for such an effect. For $\psi > \psi_1$, the experimental $\lambda_\perp$ values are lower for negative than for positive particles, in agreement with computer calculations.

The doughnuts have a considerable influence on the transmission and multiple-scattering distributions, as shown above. In figs. 6-9 were shown the transmitted intensity for particles scattered less than a certain cut angle α. In general, the distributions consisted of a peak around the crystal axis, surrounded by a broad dip. This dip is caused by the doughnuts as particles forming the doughnuts will leave the crystal at a large total scattering angle. They will thus be excluded by means of the small-angle scattering criterion as long as the cut angle α is small compared to the doughnut radius but still comparable to

the multiple-scattering angle. In figs. 8e, b, and f, α is varied from ψ_1 to $\psi_1/4$ for 15-GeV/c protons transmitted through the 0.7-mm germanium crystal. In fig. 8e, the dip is most pronounced because $\alpha = \psi_1$ reduces the doughnut more than the random region. The influence of the reduction of α, as is shown in figs. 8b and f, will reduce the random intensity rather than the doughnut region; hence the dip will disappear, as is also seen in fig. 8.

The variations in multiple scattering (cf. figs. 12 and 13) for both positive and negative particles are all caused by the doughnuts. However, this type of scattering is different from normal multiple scattering because here the angle between projectile and axis is conserved, whereas normal multiple scattering will change this angle, i.e., the radial distribution of the doughnut is smeared out.

For incident angles $\psi < \psi_1$, the radial distribution of the particles in the doughnut is governed by (i) the surface transmission at the front and back surfaces of the crystal, and (ii) diffusion in transverse energy in the crystal. The surface transmission at the front surface determines the initial transverse energies in the crystal, where $E_\perp$ is distributed between $\frac{1}{2}pv\vartheta_{in}^2$ and $\frac{1}{2}pv\psi_1^2$, with a peak around the former value since $U(r)$ is flat over most of the region. The maximum exit angle for a particle to the crystal is given by $\vartheta_{exit} = \sqrt{E_\perp/E}$, and

as the surface-transmission angle is peaked around this value for each $E_\perp$, the radial distribution for angles larger than ϑ_{in} is determined by the distribution in $E_\perp$ in the crystal, which, in turn, was governed by surface transmission at the front of the crystal. The radial distribution for angles smaller than ϑ_{in} is determined by the surface transmission at the back surface since here the potential $U(r)$ at the exit point has to be subtracted, i.e., $\vartheta_{exit} = \sqrt{E_\perp - (U(r)/E}$. This means that some particles come out with small angles to the axis because at the point of exit, they happen to be rather close to the axis, thereby having a rather high potential energy. In fig. 15 (left-hand side) is clearly seen that the intensity distributions 90° and 180° (in azimuth) away from the beam are steepest on the axis side. This reflects the fact that the diffusion in transverse energy for positive particles with low transverse energy is low, whereas particles with high transverse energy have a strong diffusion, as for random particles. Well-channeled negative particles, on the other hand, experience increased diffusion in transverse energy, which explains the tendency to a peak formation along the axial direction. However, in the present experiment, the angular resolution of the detecting system is not good enough for a detailed investigation of this problem.

The intensity in the doughnut is found to vary considerably with azimuthal angle. In fig. 17 is shown the intensity variation as a function of azimuthal angle for 15-GeV/c protons transmitted through the 0.7-mm germanium crystal. The incident angle was between ψ_1 and $2\psi_1$ with a spread in azimuth of 30°. As shown in the figure, pronounced minima occur for directions equivalent

to low-index planes. The effect simply arises because the transverse plane does not consist of randomly placed strings but rather of an ordered lattice of strings. When in the transverse plane a particle is scattered off the string into a low-index planar direction, the subsequent collision will be with atoms in the nearby string; the impact parameter will be small so that the particle will be scattered away from this direction. This effect is called "blocking" in the transverse plane and is equivalent to normal blocking in the three-dimensional crystal (see below). The widths and depths of these blocking dips should be larger, the stronger the planes, which is in qualitative agreement with our results. Once again, the angular resolution of the detecting system is comparable to the planar channeling angle ψ_p, which smears out the effect.

4.4 Binary-collision calculations

In order to derive more quantitative results from the classical theory, computer simulations of the doughnut formation for 15-GeV/c protons and π^- were performed. In figs. 18 and 19 is shown a comparison between calculated (18a and 19a) and measured doughnuts. In the calculations, a parallel beam is incident on a germanium crystal with an angle of incidence to the <110> axis of $2\psi_1$ for protons and $3\psi_1$ for π^-. In the experiment, the incident angle has a radial spread of 0.05 mrad and a spread in azimuth of 30°. Due to computer-time limitations, the calculations were performed for crystals somewhat thinner than that used experimentally. The radial spread of the doughnuts is larger for the experimental than for the calculated distributions due

to (i) the angular spread of the incident beam, (ii) the experimental angular resolution ($\sim 0.3\psi_1$), and (iii) to dechanneling in the thicker crystal.

The problem of equalization in the doughnut and the radial spread for protons and π^- can also be investigated from these computer calculations. In fig. 20 are shown the results for incident angles ψ equal to ψ_1 (a), $2\psi_1$ (b), and $3\psi_1$ (c), and for increasing crystal thickness (the thickness in μ is indicated in the upper part of the figure). In fig. 20a, the equalization is obtained after ~ 10 μ for protons and a somewhat larger thickness for π^-. This is in good agreement with Lindhard's estimate for $\lambda_\perp$ which, for the present case, is 10 μ. From the radial distribution is seen that the negative particles are preferentially scattered towards smaller ψ values, thereby filling up the intensity dip around the axis and eventually giving rise to a distribution with its maximum in the axis direction. The radial scattering for the protons is seen to be much smaller, and the doughnut distribution is conserved in the entire crystal. These results are in good agreement with the experimental results shown in fig. 15. Figures 20b and c show that now the $\lambda_\perp$ values are somewhat smaller for negative than for positive particles, in contrast to incident angles $\psi \lesssim \psi_1$. Several authors have used computer calculations based on binary collisions to study the influence of doughnuts on transmission yields[20].

Since the computer calculations seem to reproduce the rather complex angular distributions behind the crystals for different incident angles, we feel that we may have some confidence in the predicted impact-parameter distributions obtained from the

programme. In fig.21 are shown impact-parameter distributions for positive particles (normalized to random) for three different angles, $\psi_{in} \approx 0$ (a), $\psi_{in} = \frac{1}{2}\psi_1$ (b), and $\psi_{in} = \psi_1$ (c). It is clearly seen that positive particles are kept away from the string. For increasing incident angles, the distributions gradually approach random. For $\psi = \frac{1}{2}\psi_1$ (b), the effect is still rather pronounced, and for $\psi = \psi_1$, the probability that protons will hit the nuclei is still expected to be somewhat reduced. Corresponding results for 15-GeV/c π^- are displayed in fig. 22. Well-aligned negative particles are very likely to hit nuclei in the string, whereas normal scattering is expected for incident angles larger than the critical angle ψ_1.

4.5 Dechanneling

For MeV particles, dechanneling has been subject to rather intensive theoretical and experimental investigations. Most of the work has concentrated on the problem of finding the distribution $g(E_\perp,z)$ in transverse energy as a function of depth in the crystal. For clean and perfect crystals, $g(E_\perp,0)$ is sharply peaked around $\frac{1}{2}pv\vartheta_{in}^2$ because the influence of surface transmission is rather small (see above). As the beam proceeds into the target, the development of $g(E_\perp,z)$ will at first be dominated by electronic multiple scattering. With increasing transverse energy, the nuclear multiple scattering plays a growing and, eventually, a dominant role. This increase in $E_\perp$ is by nature a random-walk process and can be approximately described by a diffusion equation,

$$\frac{\partial g(E_\perp,z)}{\partial z} = \partial/\partial E_\perp A(E_\perp) D(E_\perp) \partial/\partial E_\perp \frac{g(E_\perp,z)}{A(E_\perp)} \quad , \qquad (11)$$

where $A(E_\perp)$ is the accessible area in the transverse plane for a projectile with transverse energy $E_\perp$ and $D(E_\perp)$ is the diffusion function. This model was used by Bonderup et al.[25] in their calculations of transverse-energy distribution as a function of crystal depth. We have

modified the model slightly to include relativistic effects in the multiple-scattering-dependent diffusion function. This is mainly accomplished by replacing the rest mass appearing in the non-relativistic formulas by the relativistic mass $m_o/\sqrt{1-v^2/c^2}$. So far,

most experimental investigations of dechanneling have been based on measurements of the minimum yield for wide-angle scattering. Few measurements of $g(E_\perp, z)$ have been performed in the MeV region where perfect, thin crystals and detailed angular scans behind the crystals are required[26]. However, for the present experimental arrangement, such investigations are very simple and attractive. In figs. 23 and 24 is shown the transmission yield of 15-GeV/c protons and π^- traversing 0.3-, 0.7-, and 4.2-mm germanium crystals. The results are plotted as a function of ψ^2, where ψ is the angle between the exit direction and the <110> axis; hence the obtained distributions can be compared directly to $g(E_\perp, z)$. Plots a-f correspond to a stepwise increase of $\frac{1}{4}\psi_1$ in the incident angle. Unfortunately, the overall angular resolution of the detection

system is only between $\frac{1}{3}\psi_1$ and $\frac{1}{2}\psi_1$ (see table 2) so that for incident angles between $\frac{3}{4}\psi_1$ and ψ_1 (figs. 23d and 24d), a considerable number of random particles are present. For protons in general, it is seen that for incident angles up to $\sim\frac{3}{4}\psi_1$, the transmitted yield is nearly independent of crystal thickness, showing little dechanneling even for the 4.2-mm crystal. These results have been compared to calculations based upon the diffusion model. The results of such calculations are also shown in figs. 23b and f. The overall agreement is fair even for incident angles above ψ_1, where the model is not expected to be favourable. The experimental peak heights are lower than the calculated ones, which is mainly caused by angular resolution.

It is also seen that dechanneling depends very much on the incident angle. Large dechanneling takes place for incident angles close to ψ_1, and now there is a marked difference between the different crystal thicknesses. For incident angles larger than ψ_1, a channeled part of the transmitted beam is still present, mostly due to the rather poor angular resolution. It should be noted that generally, the influence of increasing crystal thickness is an <u>increase</u> in the average transverse energy $E_\perp$ but a decrease in the most probable $E_\perp$, which is in agreement with general statistics.

Figure 24 shows the same experiment but for 15-GeV/c π^-. In general, the dechanneling is much stronger, as expected, and a large difference is seen for the three different crystals. In practically all cases, the maximum of the distribution lies around

the axis, reflecting the fact that well-channeled negative particles diffuse very quickly in transverse-energy space. For the 4.2-mm crystal, only ∿7% of the transmitted beam belongs to the channeled part ($\psi_{exit} < \psi_1$) independent of incident direction. In fig. 25, the channeled part is plotted as a function of incident angle and crystal thickness for protons and π^-. For protons, the three crystals yield nearly identical curves which, in turn, shows that the dechanneling is small. The ∿25% reduction in channeled fraction for well-aligned particles stems from the detector resolution, which caused a minimum angular step size of $\frac{1}{4}\psi_1$. A more detailed calculation of this type is made in connection with the wide-angle scattering experiments (see below).

Recently it has been discussed extensively whether channeling could be utilized as a tool for "beam cooling", i.e., an overall reduction in the transverse energy of the beam, keeping its spatial confinement. From the present experiments, it is seen that for negative particles, only a very small portion of the beam obtains a reduced transverse energy $E_\perp$.

4.6 Wide-angle scattering

In the very detailed investigations of the influence of channeling on close-encounter processes for MeV particles, Rutherford scattering has been widely used. Mostly because the FWHM of the channeling dips, $\Delta\psi$ can be compared to the theoretical ψ_1 values in a straightforward way. Both theoretically and experimentally[27] it is found that

$$\Delta\psi = k(\rho)\psi_1 ,$$

where k is a function of the thermal vibrational amplitude. For shallow depths in most crystals, k is between 1.5 and 2. To a first approximation, the minimum yield χ_{min} for this dip is equal to $Nd\pi\rho^2$ (Nd is the number of strings per unit area). For greater depths in the crystal, this minimum yield increases due to the onset of dechanneling, as discussed above.

In figs. 26 and 27 is shown the normalized wide-angle scattering yield for 15-GeV/c protons and π^- incident on the 4-mm germanium crystal. The criterion for accepting a wide-angle scattering event is that the scattering angle should be larger than the cut angle α, where α should be chosen large enough to ensure a close-encounter process. However, because of lack of intensity for large values of α, a compromise, yielding good statistical accuracy, was necessary. The random multiple scattering in the present case is 0.5 mrad so that a cut angle of $\sim$2 mrad would be reasonably outside the multiple-scattering distribution and also much larger than ψ_1 (0.18 mrad). However, the strong influence of doughnuts at high energies means that it is necessary to use larger α values because doughnut scattering results in large scattering angles, but the impact-parameter distributions for such collisions are still different from those in amorphous targets, as shown above. Thus a value of α = 3 mrad was used for the axial case. For planes, where no doughnut formation exists, much smaller α values can be used, which gives much better statistics. For axial-channeled protons, a pronounced dip (8% of normal yield) is obtained for incident angles close to the <110> axis. The FWHM is seen to be

$1.5\psi_1$, in good agreement with the above estimate. It should be pointed out that since we have no depth resolution, the result represents the scattering yield averaged over the entire thickness of the sample. In the same figure is plotted (solid curve) the calculated dip in yield (averaged over the crystal), using the Lindhard theory. In the calculations, dechanneling is taken into account, using the diffusion model of Bonderup et al.[25]. Here it should be noted that dechanneling alone would give a minimum yield of 3%. The solid curve represents the result of folding in a Gaussian curve representing the angular resolution of the incident beam and the effect of a rather large angular step size. This procedure raises the minimum yield to 9%, so evidently our limited angular resolution plays an important role in the determination of the experimental angular yields. The theoretical FWHM is ∿30% larger than the experimental width.

In fig. 27 are shown the normalized wide-angle-scattering results as a function of incident angle to the <110> axis for 2- and 6-GeV/c protons and π^+ transmitted through the 4.2-mm germanium crystal. Very pronounced dips are obtained for 6 GeV/c with FWHM values around $1.5\psi_1$. The moderate dip at 2 GeV/c is caused by poor detector resolution.

For π^- (fig. 28), an increase in yield is found for incident angles close to the <110> axis. This peak is much narrower than the proton dip, which is in good agreement with MeV electron-channeling results, where it is found that the FWHM $\Delta\psi$ is equal to $0.65\psi_1$ (ref. 17). Due to poor statistics in the present case, we shall refrain from any detailed analysis

of the peak in yield. The moderate rise in yield is due to the strong dechanneling for negative particles (see above). From electron-channeling experiments and binary-collision calculations, one would expect peak values a factor of 3-5 above normal yield for thin crystals, but in this type of scattering experiments, thin crystals would require a fast hardware selection to reduce the running time; however, this will be arranged in a forthcoming experiment.

As discussed above, the crystal planes also have a steering effect. In fig. 29 is shown the normalized wide-angle-scattering (α = 0.6 mrad) intensity around the {111} plane for 15-GeV/c protons incident on the 4.2-mm germanium crystal. A dip down to 60% of normal yield is obtained, but now the restricted angular resolution has a severe influence on the minimum because the overall resolution is equal to the planar-channeling angle ψ_p, which, for the present case, is 0.6 mrad. Hence the FWHM is mostly determined by resolution.

The influence of channeling on nuclear reactions induced by strongly interacting projectiles is expected to be the same as that for wide-angle scattering since both processes require impact parameters much smaller than the minimum distance ($\sim\rho$) from the string of channeled particles. In fig. 30 is shown the variation in intensity around the <110> axis of 15-GeV/c protons and π^- having suffered an extraordinarily large energy loss. The normal average energy loss would be 2.3 MeV for the crystal studied (4.2-mm germanium), and here we have used 5.4 MeV as the rather arbitrary energy loss, above which it is called

"large energy loss". In ref. 7 it is shown that such a large energy loss is directly connected to nuclear-reaction processes, where more particles are produced for which the total energy loss is integrated by the target detector. For protons, a very pronounced dip down to 10% of normal yield is obtained, which is quite similar to the wide-angle-scattering dip shown in fig. 26.

For π^- we find an increase in yield for incident angles around the <110> axis, but the width of the peak is much broader than that obtained for wide-angle scattering (fig. 28). To some extent, this difference is caused by the increased electronic-energy loss for channeled π^-. The influence of this effect was evaluated by requiring that the energy loss be large and that the particle hits DC5. By this test, only part of the increased yield could be accounted for. Due to poor statistics, we shall refrain from any further analysis of the precise form and magnitude of the enhancement of these peaks.

Since the prospect of increasing reaction rates is very intrigueing and since we cannot solve the problem in any decisive way from the data available in the present experiment, we have made more detailed investigations of the problem, using the binary-collision calculations. Figure 31 shows the expected impact-parameter distribution for 15-GeV/c π^- mesons after their passage through 20 and 300 μ of the <110> germanium crystal. It is obvious that the projectiles have a much increased flux near the string, and for a well-aligned π^- and a thin crystal, we should then expect a strongly enhanced probability for small impact-parameter processes.

4.7 Blocking

When positive particles are emitted from radioactive nuclei on normal lattice sites in single crystals, the emission yield shows very pronounced and sharp minima whenever the emission direction is parallel to a low-index planar or axial direction. This is a result of the string potential that deflects the emitted ions away from the axis. This shadowing effect of the axis is usually called the blocking effect. For negative particles, pronounced maxima are found under the same emission conditions[27].

The emission case can be simulated by using an energetic beam incident on a crystal and then detecting those particles emerging from the crystals that have been scattered through a large angle. The large-angle single scattering ensures that the particles have been close to the nuclei, and thereby a radioactive-emission experiment is simulated. Also multiple-scattering distributions will show pronounced dips (peaks) whenever a crystal axis or plane is oriented inside the multiple-scattering distribution.

By a reversibility argument, Lindhard[16] has shown that the angular yield in the blocking experiment should be identical to the wide-angle scattering yield previously discussed if energy loss may be neglected for the trajectories connecting the external beam (either entering or exiting) with the position of the scatterer in the crystal. This result is based upon the fact that the probability of hitting a lattice atom for a particle incident on a crystal in a specific direction is equal to the probability for the particle to escape from the crystal in that

direction when emitted from the lattice atom. The probabilities are here taken relative to the case of an amorphous target.

Figure 32 shows a scatter plot of the transmitted intensity for 15-GeV/c protons transmitted through the 4.2-mm germanium crystal. In the present experiment, the <110> axis was tilted away from the central beam. It is clearly seen that the presence of the axis results in a dip along this direction because the direction is blocked. Perpendicular scans (scan directions indicated in the figure) through the dip are also shown in fig. 33. These data are shown unnormalized because the results may be influenced by doughnut formation, so it is not well justified to compare the minimum yield and width with the wide-angle scattering results.

A more direct way of investigating the blocking effect is to study the variation in emission yield around the <110> axis of those particles produced in the induced nuclear reactions. These events are identified by registering "large energy-loss" events defined as above. Figure 34 shows the intensity distribution around the <110> axis for "large energy-loss" events. The data are obtained from ring-integration centered on the <110> axis in order to get better statistics. The dip in yield is down to ∿20% of normal yield and the FWHM is $\sim 1.5\psi_1$, in good agreement with the results obtained for close-encounter processes. The minimum yield is somewhat uncertain due to the large angular steps that were necessary to obtain reasonable statistics.

5. Conclusion

From the data and analyses presented, several conclusions may be drawn. Thus channeling conditions may be maintained for both positive and negative particles through thick ($\sim$4 mm), nearly perfect crystals.

In the high-energy region, channeling effects become increasingly important since multiple scattering and dechanneling decrease as $(pv)^{-1}$, whereas channeling angles only decrease as $(pv)^{-\frac{1}{2}}$. Further, it is found that channeling effects persist for angles large compared to the critical angle ψ_1.

Most scattering phenomena are changed drastically whenever crystal axes and planes are close to the incident-beam cone. Especially the doughnut formation has been found to be much more pronounced in the GeV region than at lower energies.

With regard to the theoretical description, it is found that the models developed for positive, classical particles can easily be transformed to the GeV region and describe most experimental results very well.

Our confidence in the theoretical description opens up a new experimental area, where the variety of particles in high-energy beams are used for special solid-state-, atomic-, and nuclear-physics investigations. Particularly the possibility of varying the impact-parameter distributions is very intrigueing. As the relativistic γ values vary over two orders of magnitude in most secondary beams, the investigation of the onset of relativistic effects is very simple, and the channeling effect

can be used for discerning between contributions from close ($b \lesssim \rho$) and distant collisions, which is very important in x-ray and bremsstrahlung experiments.

ACKNOWLEDGEMENTS

The authors are grateful to J.U. Andersen, E. Bonderup, and J. Lindhard for fruitful discussions and helpful criticism. We are especially indebted to J.A. Golovchenko, who played an active part in the early stages of our high-energy channeling experiments. Alice Grandjean's untiring help in the preparation of the manuscript is gratefully acknowledged. The Danish participation in this collaboration was made possible by funds from the Danish Committee for Accelerator Physics and from the Danish Natural Science Research Council.

References

1) D.Allen et al., Observation of Channeling of Negative Pions of 4 GeV/c Momentum. Nuovo Cimento Lett.15 (1976) 529

2) O.Fich, J.A.Golovchenko, K.O.Nielsen, E.Uggerhøj, G. Charpak, and F.Sauli, Channeling of 1.1-GeV/c Protons and Pions. Phys.Lett.57B (1975) 90

3) O.Fich, J.A.Golovchenko, K.O.Nielsen, E.Uggerhøj, C. Vraast-Thomsen, G.Charpak, S.Majewski, F.Sauli, and J.P.Ponpon, Ionization Loss of Channeled 1.35-GeV/c Protons and Pions. Phys.Rev.Lett.36 (1976) 1245

4) H.Esbensen, O.Fich, J.A.Golovchenko, K.O.Nielsen, E. Uggerhøj, C.Vraast-Thomsen, G.Charpak, S.Majewski, F.Sauli, and J.P.Ponpon, Channeling of Protons, Pions, and Deuterons in the GeV Region. Nucl.Phys.B 127 (1977) 281

5) H.Esbensen, O.Fich, J.A.Golovchenko, S.Madsen, H.Nielsen, H.E.Schiøtt, E.Uggerhøj, C.Vraast-Thomsen, G. Charpak, S.Majewski, G.Odyniec, G.Petersen, F.Sauli, J.P.Ponpon, and P.Siffert. Channeling Effects for 15-GeV/c Negative Pions. Phys.Lett.72B (1978) 408

6) H.Esbensen, O.Fich, J.A.Golovchenko, S.Madsen, H. Nielsen, H.E.Schiøtt, E.Uggerhøj, C.Vraast-Thomsen, G.Charpak, S.Majewski, G.Odyniec, G.Petersen, F. Sauli, J.P.Ponpon, and P.Siffert, Random and Channeled Energy Loss in Thin Germanium and Silicon Crystals for Positive and Negative 2 - 15-GeV/c Pions, Kaons, and Protons. Phys.Rev.B 18 (1978) 1039

7) S.K.Andersen, H.Esbensen, O.Fich, J.Golovchenko, H.Nielsen, H.E.Schiøtt, E.Uggerhøj, C.Vraast.Thomsen, G.Charpak, G.Petersen, F.Sauli, J.P.Ponpon, and P.Siffert, Nuclear Interactions for 15-GeV/c Protons and Pions under Random and Channeling Conditions in Germanium Single Crystals. Nucl.Phys.B 144 (1978) 1

9) V.M.Golovatyuk et al., Investigation of possibility of bending and cooling of beams by single crystals. Design of new type detectors for charged particles. A Dubna Serphukov proposal

10) C.Ankenbrandt et al. Proposal to Study Channeling at Fermilab. Sept.1975

11) T.H.Braid, D.S.Gemmel, R.E.Holland, W.J.Pietsch, A.J. Ratkowski, J.P.Schiffer, T.P.Wangler, J.W.Worthington, B.Zeidman, C.T.Morris, and H.A.Thiessen, The channeling of positive and negative pions in a silicon crystal. Phys.Rev.B 19 (1979) 1

12) I.A.Grishaev, G.D.Kovalenko, and B.I.Shramenko,

Zh.Eksp.Teor.Fiz.72 (1977) 437

13) J.U.Andersen, H.Nielsen, E.Uggerhøj, J.Golovchenko, Is it possible to measure elementary particle lifetimes using blocking techniques? Aarhus preprint, to appear elsewhere

14) R.L. Walker, B.L. Berman, and S.D. Bloom, Phys.Rev. A 11, (1975) 736, and private communication.

15) M.A. Kumakhov, Phys.Status Solidi (b) 84 (1977) 41

16) J. Lindhard, K.Dan.Vidensk.Selsk.Mat.Fys.Medd. 34, No. 14 (1965); Ph. Lervig, J. Lindhard, and V. Nielsen, Nucl. Phys. A96 (1967) 481

17) E. Uggerhøj and F. Frandsen, Phys.Rev. B 2 (1970) 582; S.K. Andersen, F. Bell, and E. Uggerhøj, Phys.Rev. B 8 (1973) 4913

18) U. Schiebel, Diplomarbeit: Klassische Rechnungen zon Elektronenchanneling in MeV-Bereich (unpublished)

19) A. Breskin, G. Charpak, F. Sauli, M. Atkinson, and G. Schultz, Nucl.Instrum. 124 (1975) 189

20) A. Neufert, U. Schiebel, and G. Clausnitzer, Radiat.Eff. 26 (1976) 57; V.V. Kudrin and S.A. Vorobiev, Radiat.Eff. (1974) 145; V.V. Kudrin and S.A. Vorobiev, Radiat.Eff. (1975) 119

21) N. Bohr, K.Dan.Vidensk.Selsk.Mat.Fys.Medd. 18, No 8 (1948); W.T. Scott, Rev.Mod.Phys. 35 (1963) 2

22) D.D. Armstrong, W.M. Gibson, A. Goland, J.A. Golovchenko, R.A. Levesque, R.L. Meek, and H.E. Wegner, Radiat.Eff. 12 (1973) 143; J.S. Rosner, W.M. Gibson, J.A. Golovchenko, A.N. Goland, and H.E. Wegner, Phys.Rev. B 18 (1978) 1066

23) J.A. Golovchenko, Phys.Rev. B 13 (1976) 4672

24) J.U. Andersen and L.C. Feldman, Phys.Rev. B 1 (1970) 2063

25) E. Bonderup, H. Esbensen, J.U. Andersen, and H.E. Schiøtt, Radiat.Eff. 12 (1972) 261; H.E. Schiøtt, E. Bonderup, J.U. Andersen, and H. Esbensen, in: Atomic Collisions in Solids 2 ((1974) eds. S. Datz, B.R. Appleton, and C.D. Moak

26) M.J. Pedersen, J.U. Andersen, D.J. Elliot, and E. Lægsgaard, in: Atomic Collisions in Solids 2 (1974), eds. S. Datz, B.R. Appleton, and C.D. Moak

27) D.S. Gemmel, Rev.Mod.Phys. 46, No 1 (1974)

28) E. Uggerhøj, Phys.Lett. 22 (1066) 382; E. Uggerhøj and J.U. Andersen, Can.J.Phys. 46 (1968) 543

Figure captions

Fig.1 Three dimensional plot of the continuum potential for the <100>Cu axis. The potential-cut at the top corresponds to $E_\perp = 1/2\ p\,v\psi_1^2$. The plane half-way between top and bottom shows the accessible area for particles with an incident angle of $\frac{1}{2}\psi_1$ with respect to the axis.

Fig.2 Schematic drawing of experimental layout. The beam is defined by means of scintillation counters SC1 - 4 and the particle tracks by means of drift chambers DC1 - 5. VT 1 and VT 2 are vacuum tubes.

Fig.3 Multichannel analyzer spectrum from the target. The low-energy part comes from channeled particles, whereas the high-energy part is caused by "random" particles. The windows W_1 and W_2 are set for alignment of the crystal.

Fig.4 Alignment scans for the 0.9 mm <110> Si crystal using 15 GeV/c π^+ as beam. The two x scans and one y scan show the counts in W_1 for 10^4 events in W_2.

Fig.5 Scans through incident (full drawn) and exit (dashed curve) beam for 15 GeV/c protons transmitted through a 0.3 mm <110> Ge (a) and 4.2 mm <110> Ge (b) crystals together with 2 GeV/c protons transmitted through the 4.2 mm <110> crystal (c).

Fig.6 15-GeV/c protons incident on a 4.2 mm Ge single crystal. The picture is a reproduction of a computer output and shows the relative intensity distribution as function of incident angle to the crystal axis for particles which have been scattered less than 0.1 mrad in the crystal. Dark areas correspond to high intensity. Each point shows the

intensity in a box of 0.05 × 0.05 mrad. The position of the axis and the planes are clearly seen. Note the reduction in yield away from axis and planes for incident angles less than around 1 mrad. There are 20 000 events in the plot.

Fig.7 15-GeV/c π^- incident on a 4.2-mm Ge single crystal. Same plot and condition as in Fig.6. Here planar effects are absent but there is a peak in the axial direction surrounded by a low-intensity region. Note that the axial peak is lower than the random "plateau" far from the axis. There are 10 000 events in the plot.

Fig.8 Variation in the transmission yield as a function of incident angle (relative to < 110 > axis) for 15-GeV/c protons transmitted through 0.3 m Ge (a), 0.7 mm Ge (b), 4.2 mm Ge (c), and 0.9 mm Si (d). Together with 6 GeV/c protons (g) and 2 GeV/c protons (h) transmitted through the 4.2 mm Ge crystal. In all the above cases the cut angle α equals $\psi_1/2$. Figures e and f show the transmission yield for 15 GeV/c protons through the 0.7 mm Ge crystal but with cut angle α equal to ψ_1 and $\psi_1/4$, respectively.

Fig.9 The same type of plots as fig.8 but for 15 GeV/c π^- transmitted through 0.3 mm (a) and 4.2 mm (b) <110> Ge crystals. The cut angle α equals $\psi_1/2$.

Fig.10 Scan through the raw incident (full drawn) and exit (dashed) beam for 15 GeV/c protons transmitted through the 4.2 mm Ge crystal with the {111} plane inside the beam cone.

Fig.11 Distributions of relative transmission yield as a function of incident angle to the {111} plane (a) and the {112} plane (b) for 15 GeV/c protons incident on the 4.2 mm Ge crystal. In both cases, the cut angle α was equal to 0.05 mrad.

Fig.12 Integrated intensity distribution as a function of scattering angle for 15 GeV/c protons (a) and π^- (b) transmitted through the 4.2 mm <110> Ge crystal. In both cases are shown results from three incident-angle regions, namely for protons: 0 - 0.25 ψ_1 (▲), 3 - 3.5 ψ_1 (●), and random (o); for π^- 0 - 0.25 ψ_1 (▲), 4 - 5 ψ_1 (●), and random (o). For comparison is shown the Bohr-Williams (dashed) and Molière (full drawn) theoretical curves.

Fig.13 Angular width of multiple scattering distributions as a function of incident angle to the <110> axis for 15 GeV/c protons and π^- transmitted through 0.3 mm and 4.2 mm Ge crystals.

Fig.14 Three-dimensional scatter plots in exit-angle space of 15 GeV/c protons and π^- transmitted through a 0.9 mm <110> Si crystal. The incident beam directions are indicated (2 - 2.5) ψ_1 from the axis). The center of the plots are in the <110> axis.

Fig.15 Perpendicular scans (scan direction shown at the top) through doughnuts resulting from a narrow beam of 15 GeV/c protons (a) and π^- (b) transmitted through a 0.7 mm Ge <110> crystal. The scans are plotted as a function of exit angle relative to the <110> axis.

The figures 1 - 12 correspond to different incident directions (incident beams indicated as square boxes with error bars corresponding to detector resolution) varying from ~ 0 (1) to $3.3\psi_1$ (12).

Fig.16 Intensity in doughnut 180^0 azimuthally away from beam direction relative to intensity at the beam position for protons and negative pions at various energies and through various crystal thicknesses.

Fig.17 Plot of intensity in doughnut as function of azimuthal angle for 15 GeV/c protons transmitted through a 0.7 mm Ge crystal. The blocking effect of low-index planes is clearly seen.

Fig.18 Calculated (left) and measured (right) doughnut for 15 GeV/c protons transmitted through a 0.7 mm Ge crystal. In the calculation the beam is very narrow (marked by a black dot), whereas the experimental beam is rather broad (marked by a black streak) - and in fact broader than indicated because of angular resolution.

Fig.19 The same as fig.19, but for π^-.

Fig.20 Results of computer simulations for 15 GeV/c protons and π^- traversing increasing thicknesses of Ge. The incident angle to the axis is ψ_1, $2\psi_1$, and $3\psi_1$, respectively, in figs. 20a,b,c. Clearly, for small

angular incidence the protons attain equalization on the shorter distance, whereas for larger angles of incidence, π^- seem to attain equalization on the shorter distance.

Fig.21 Impact parameter distribution for various incident angles, from computer simulation. The distributions are normalized to random and show that particles have in general small probabilities for close encounters.

Fig.22 Same af fig. 21 but for negative particles. There is only a clear enhancement for well-channeled particles, which exhibit a strong increase in the probability of close encounters.

Fig.23 Distribution in "transverse energy" (which is proportional to ψ^2) of 15 GeV/c protons transmitted through 0.3 mm, 0.7 mm, and 4.2 mm Ge crystals. Plots a) to f) give results for particles with increasing angle of incidence to the <110> axis. The full-drawn curves are for the 0.3 mm, the dashed curves for the 0.7 mm, and the dot-and-dash curves for the 4.2 mm crystal. In plots b) and f) are shown examples of a comparison with theory (smooth curves). The agreement is satisfactory for the small incidence angle, but only fair for the larger angles of incidence.

Fig.24 Same as fig.23, but for π^-, with the exception that there is no theory to compare with.

Fig.25 Fraction of particles still channeled after having traversed 0.3 mm, 0.7 mm, and 4.2 mm Ge crystal, for 15 GeV/c protons (a) and π^- (b). For positive well-channeled particles, the dechanneling is seen to be very small, whereas dechanneling for negative particles is very strong.

Fig.26 Normalized (to random incidence) yield of wide-angle-scattering as function of incident angle to the <110> axis for 15 GeV/c protons in the 4.2 mm Ge crystal. Experimental points and a theoretical curve. The latter takes into account dechanneling and angular resolution of the system.

Fig.27 Experimental normalized wide-angle scattering yields as function of incident angle to the <110> axis in Ge for 6 and 2 GeV/c protons and π^+.

Fig.28 Experimental normalized wide-angle-scattering yield as function of incident angle to the <110> axis in Ge for 15 GeV/c π^-. The curve is drawn by eye through the points. Within a narrow region ($\psi < \frac{1}{3}\psi_1$), there is a strong increase in yield, as expected.

Fig.29 Experimental normalized wide-angle-scattering yield as function of incident angle to the {110} plane in Ge for 15 GeV/c protons.

Fig.30 Experimental probability for 'large energy loss' as function of incident angle to the <110> axis in Ge for 15 GeV/c protons and π^-.

Fig.31 Computer simulation. Predicted impact-parameter distribution of 15 GeV/c π^- after having penetrated 19 μ (A), and

~~300~~ 150 μ (B) in a perfect Ge crystal, for an incident angle of ~~0.025~~ 0.04 $\cdot \psi_1$ to the <110> axis.

Fig.32 Scatter plot of the transmitted intensity for 15 GeV/c protons incident on the 4.2 mm Ge crystal. The <110> axis was tilted away from the central part of the beam and the position of the axis is at the intersection of the the two scan directions indicated.

Fig.33 Scans through the distribution shown in fig.32. Scan 1 is through beam and axis, and scan 2 is perpendicular to scan 1. In both scans the position of the axis is clearly indicated by the minimum in transmission intensity.

Fig.34 Experimental "blocking effect". The yield of 'large energy loss' processes as function of particle exit angle to the <110> axis in Ge. The crystal was 4.2 mm thick, and the particles were 15 GeV/c protons.

Table I

The critical angle ψ_1 in mrad. The tabulated values are for $\beta = 1$.

	2 GeV/c	6 GeV/c	15 GeV/c
Si<110>	0.32	0.19	0.12
Ge<110>	0.48	0.28	0.18

Table II

Calculated ($\beta = 1$) and measured angular resolutions in mrad

Experiment	0.3 mm, 0.7 mm Ge, and 0.9 mm Si			4.2 mm Ge		
Energy	2 GeV/c	6 GeV/c	15 GeV/c	2 GeV/c	6 GeV/c	15 GeV/c
$\sigma_{incident}$ (calculated)	0.55	0.18	0.07	0.25	0.08	0.04
σ_{exit} (calculated)	0.05	0.03	0.02	0.05	0.03	0.02
σ_{total} (measured)	0.67	0.23	0.70	-	0.11	0.06

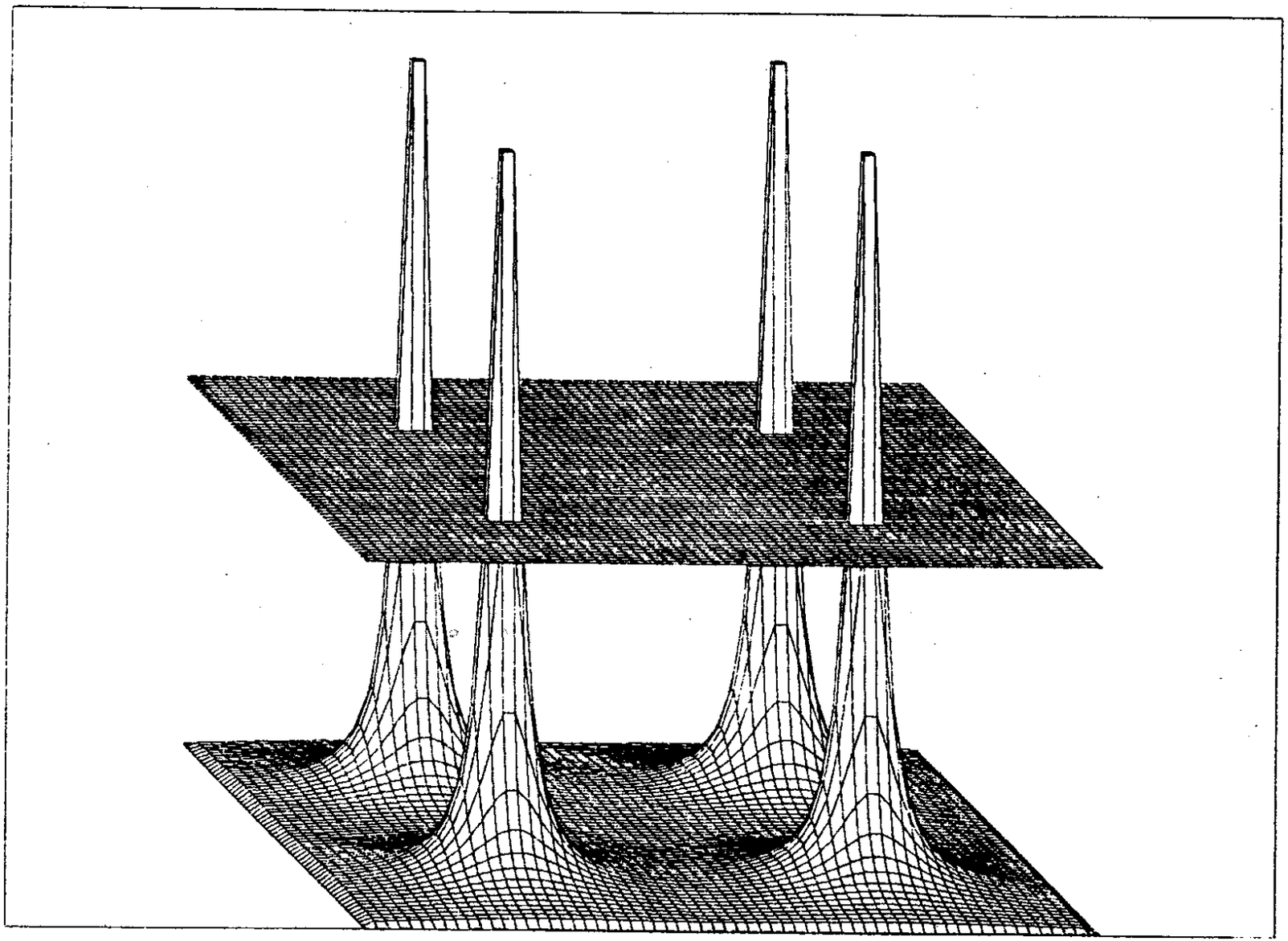

Fig. 1

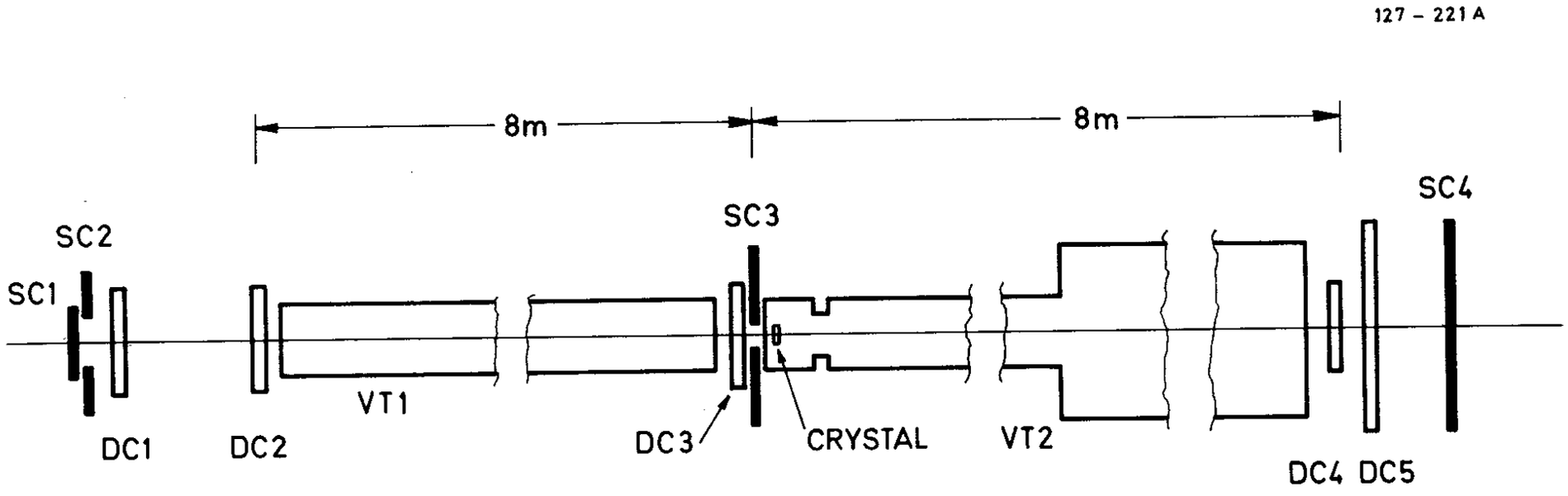
127 - 221 A
8m
8m
SC4
SC3
SC2
SC1
VT1
DC1
DC2
DC3
CRYSTAL
VT2
DC4
DC5

Fig.2

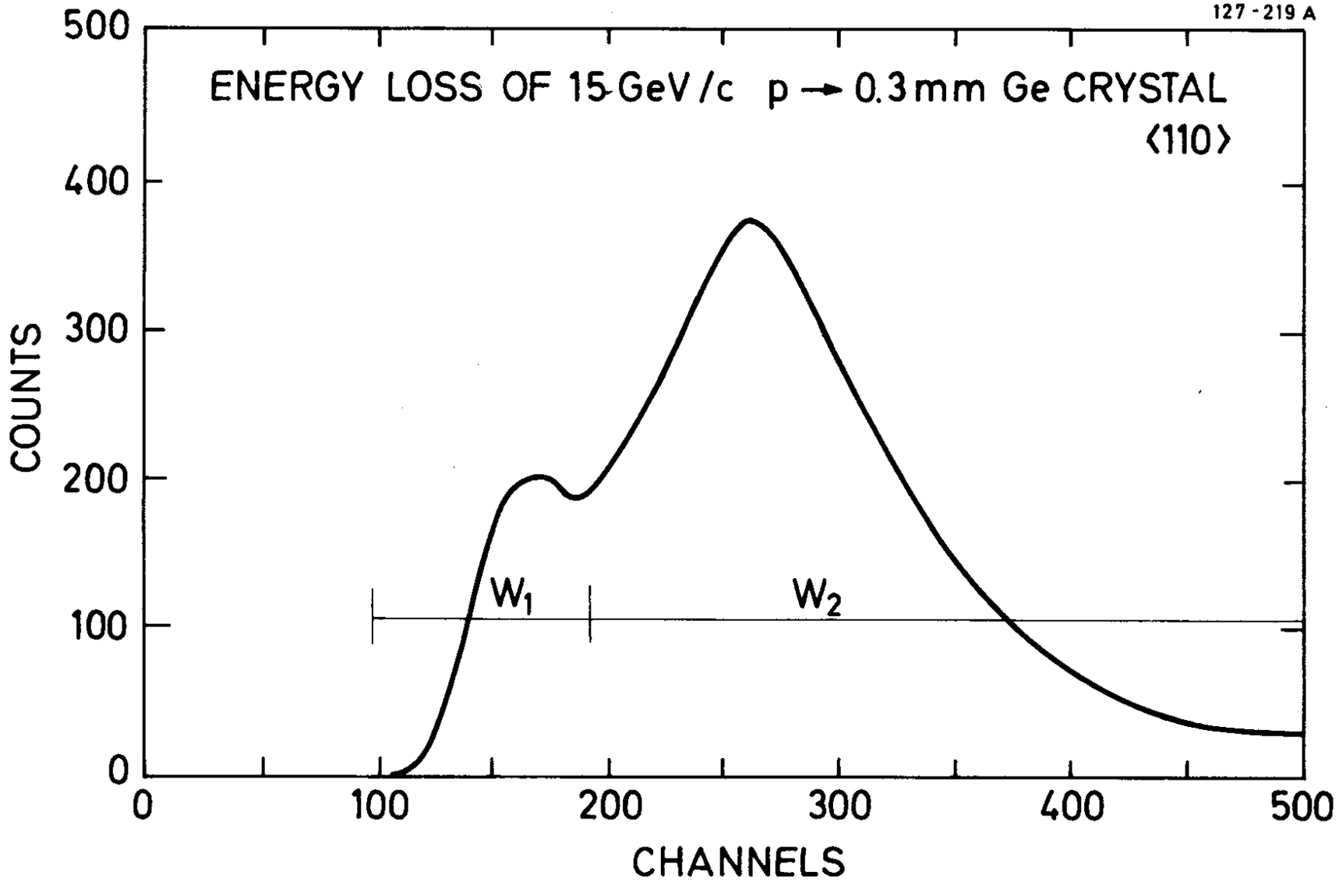
127-219 A
ENERGY LOSS OF 15 GeV/c p → 0.3 mm Ge CRYSTAL
⟨110⟩
COUNTS
CHANNELS
W1
W2
0
100
200
300
400
500

Fig.3

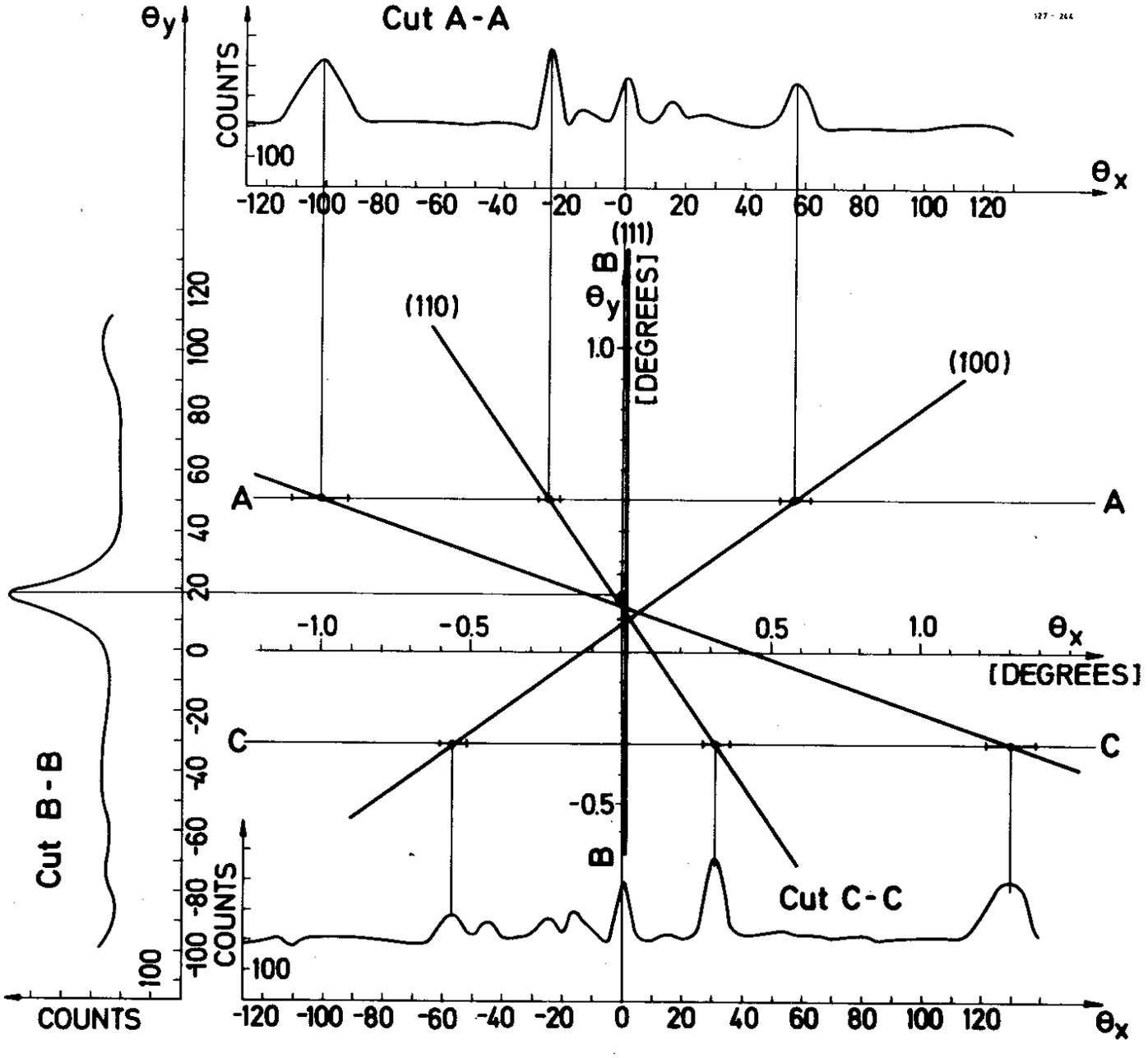
Cut A-A
Cut B-B
Cut C-C
COUNTS
100
θ_y
θ_x
(111)
(110)
(100)
A
B
C
1.0
-0.5
[DEGREES]
-120 -100 -80 -60 -40 -20 -0 20 40 60 80 100 120
-1.0 -0.5 0.5 1.0

Fig.4

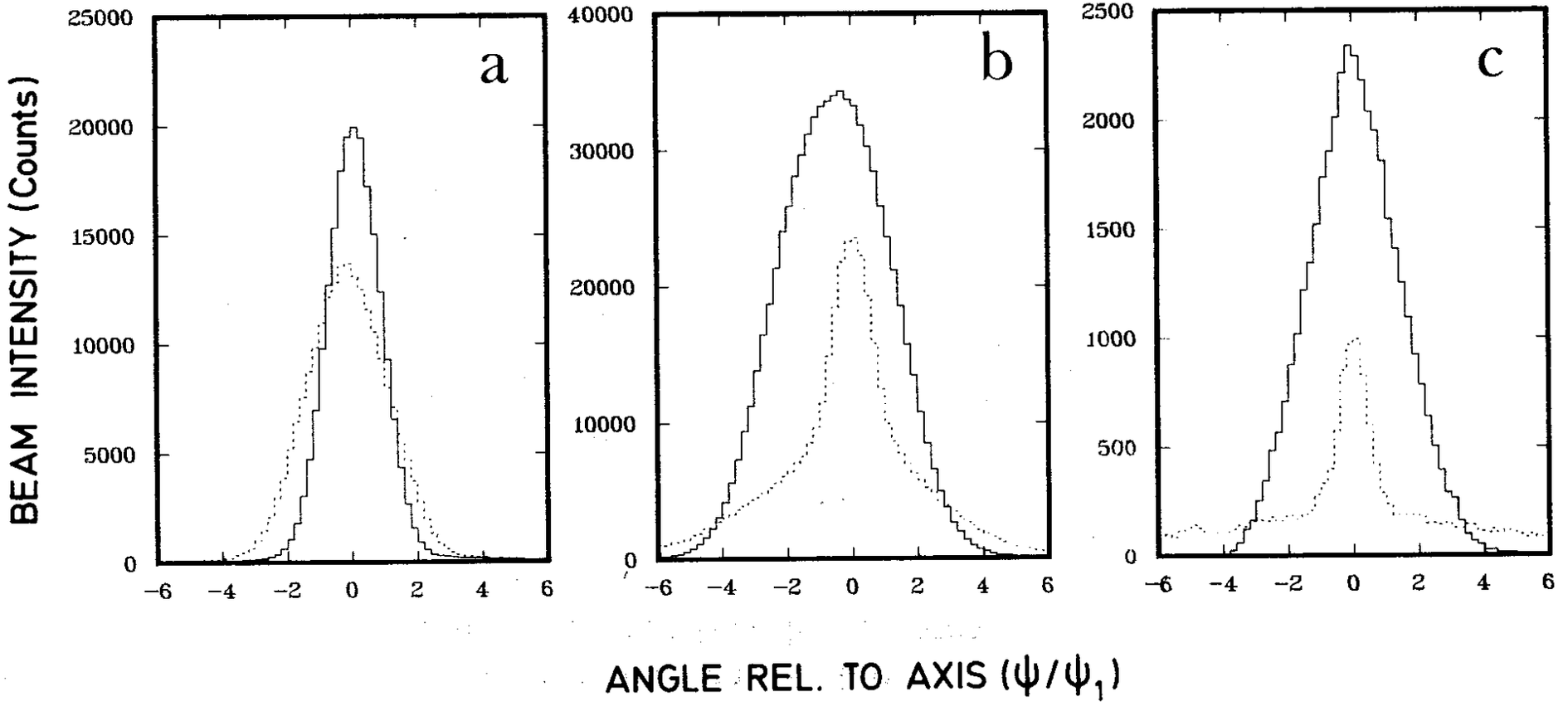
BEAM INTENSITY (Counts)
25000
20000
15000
10000
5000
0
a
40000
30000
20000
10000
0
b
2500
2000
1500
1000
500
0
c
−6 −4 −2 0 2 4 6
ANGLE REL. TO AXIS (ψ/ψ1)

Fig.5

15 GeV/c p → 4.2 mm Ge ⟨110⟩
Scattering angle less than 0.1 mrad

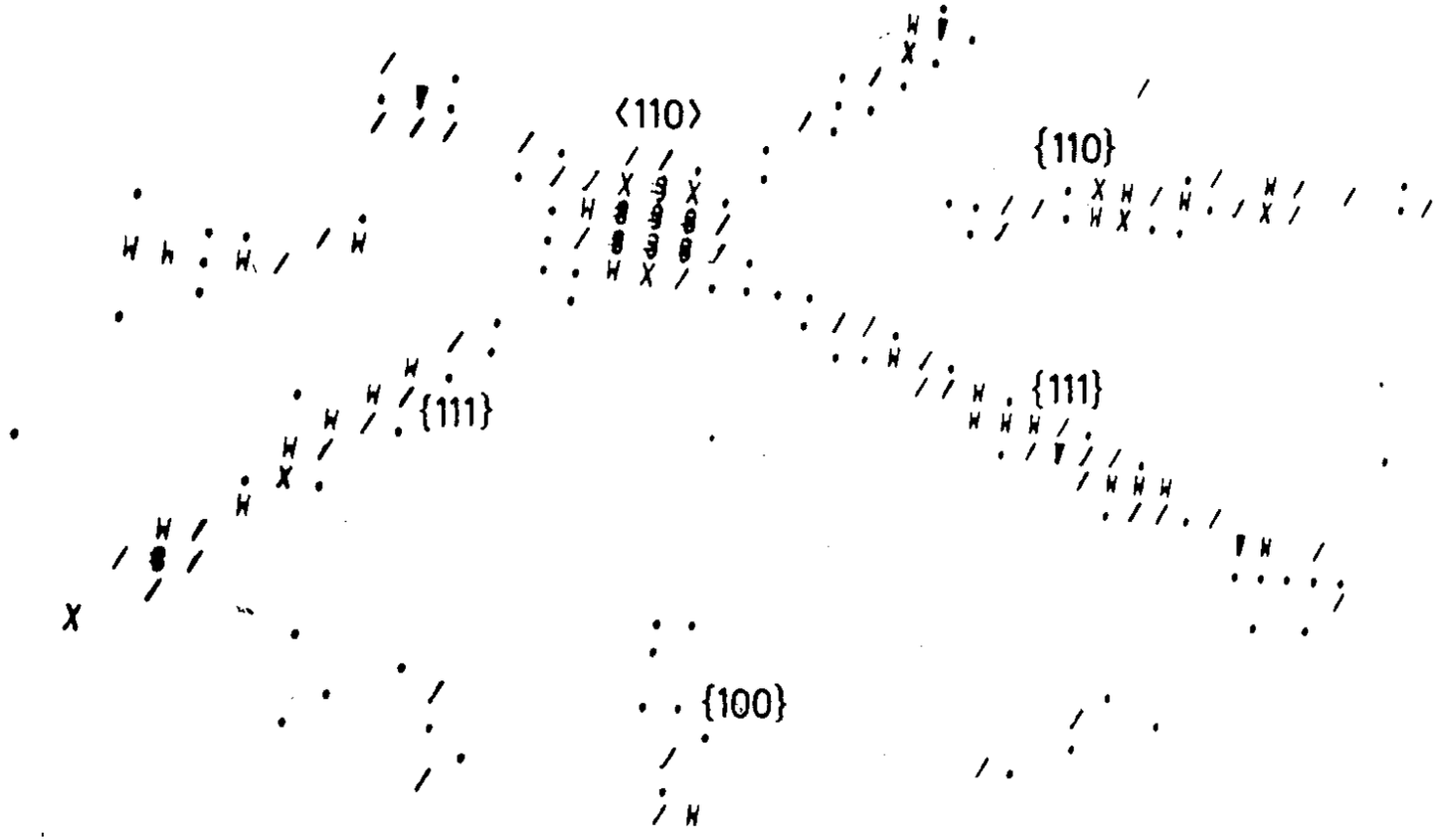

Relative intensities: • ≥ 2 , / ≥ 3 , W ≥ 4 , X ≥ 5 , ▼ ≥ 6 , ■ ≥ 7

Fig.6

15 GeV/c $\pi^- \rightarrow$ 4.2 mm Ge ⟨110⟩
Scattering angle less than 0.1 mrad

Relative intensities: • ≥ 2, / ≥ 3, W ≥ 4, X ≥ 5, ▼ ≥ 6, ■ ≥ 7

Fig.7

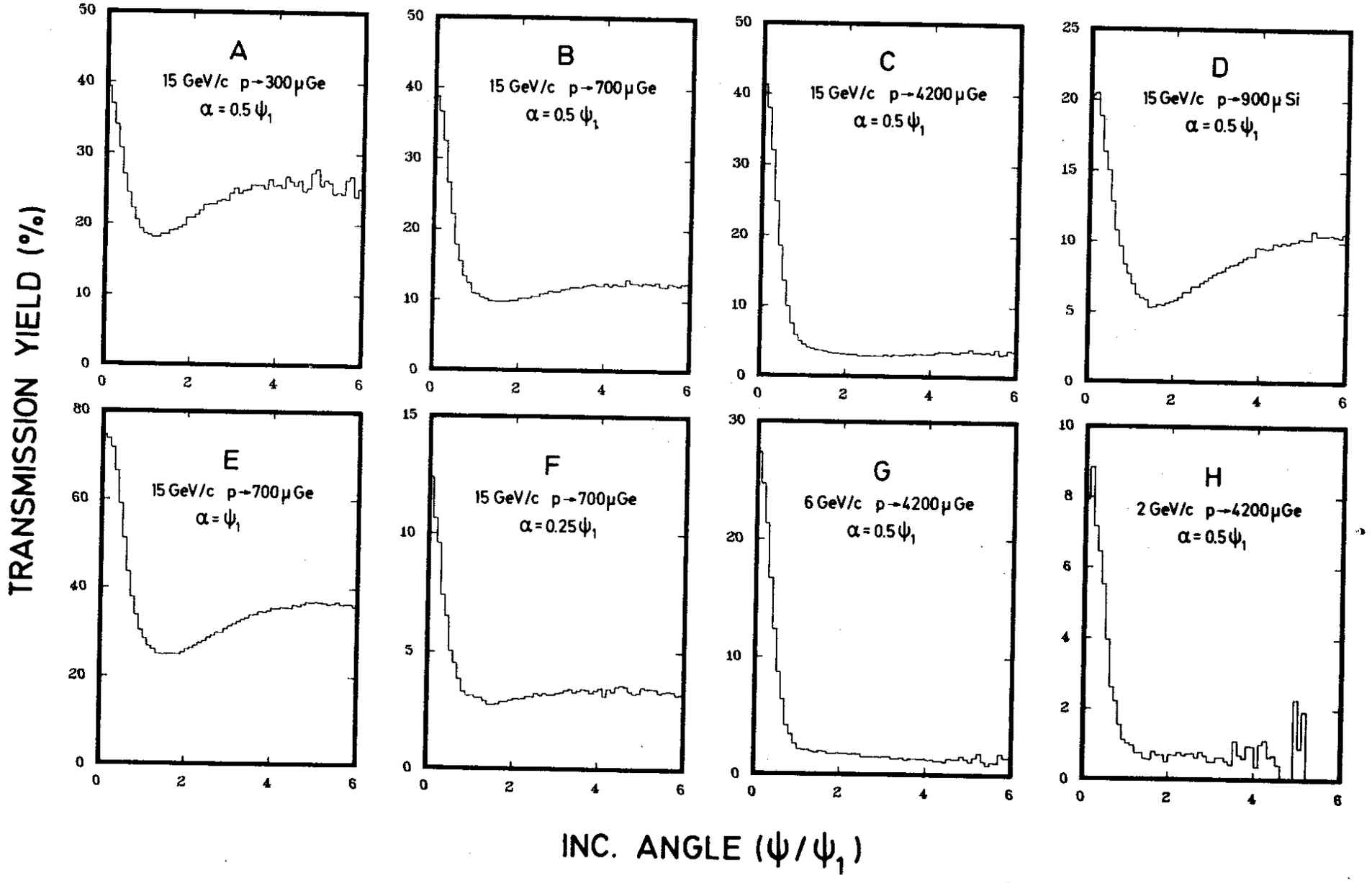
A
15 GeV/c p→300μGe
α = 0.5 ψ1
B
15 GeV/c p→700μGe
α = 0.5 ψ1
C
15 GeV/c p→4200μGe
α = 0.5 ψ1
D
15 GeV/c p→900μSi
α = 0.5 ψ1
E
15 GeV/c p→700μGe
α = ψ1
F
15 GeV/c p→700μGe
α = 0.25 ψ1
G
6 GeV/c p→4200μGe
α = 0.5 ψ1
H
2 GeV/c p→4200μGe
α = 0.5 ψ1
TRANSMISSION YIELD (%)
INC. ANGLE (ψ/ψ1)

Fig. 8

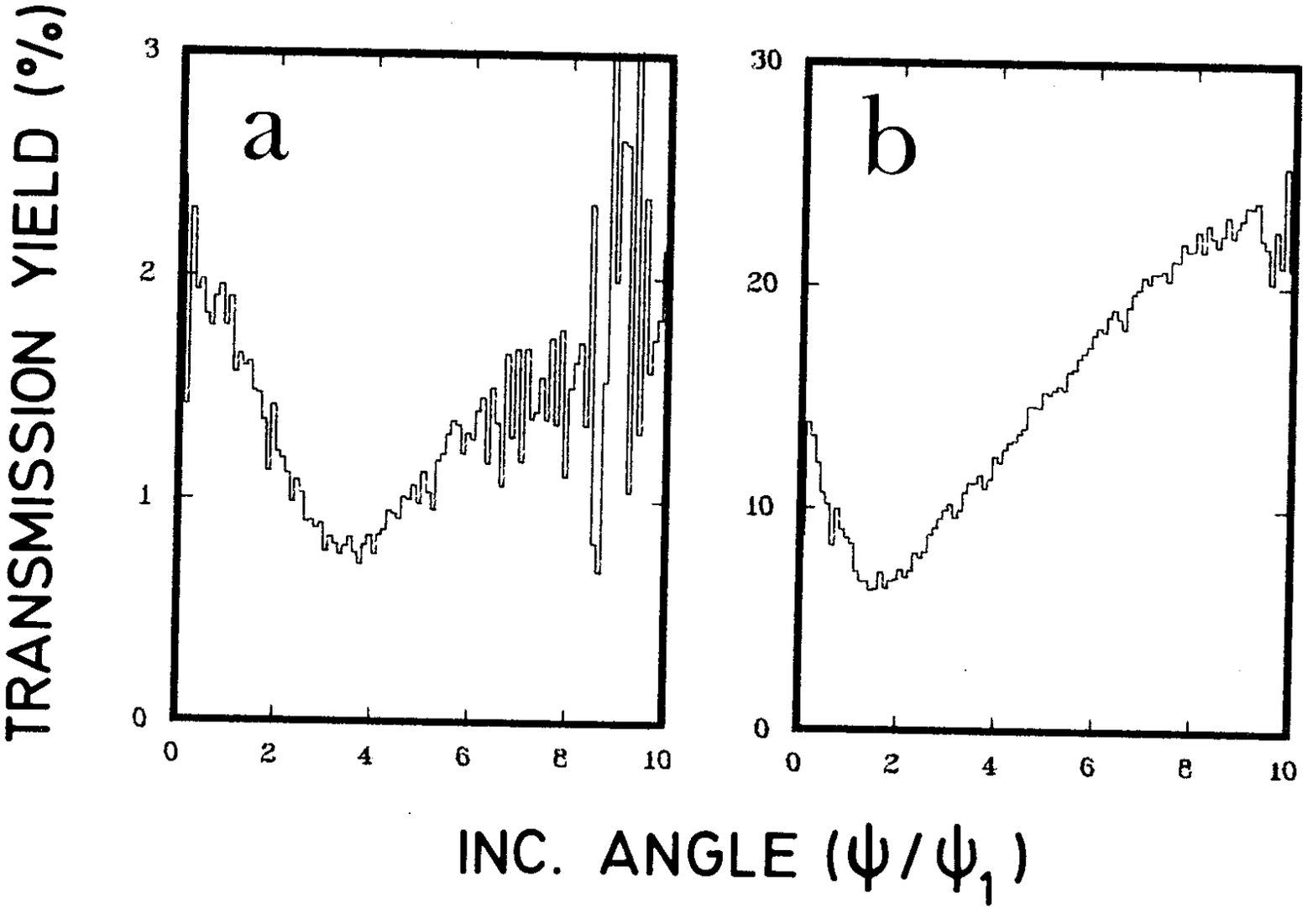

Fig. 9

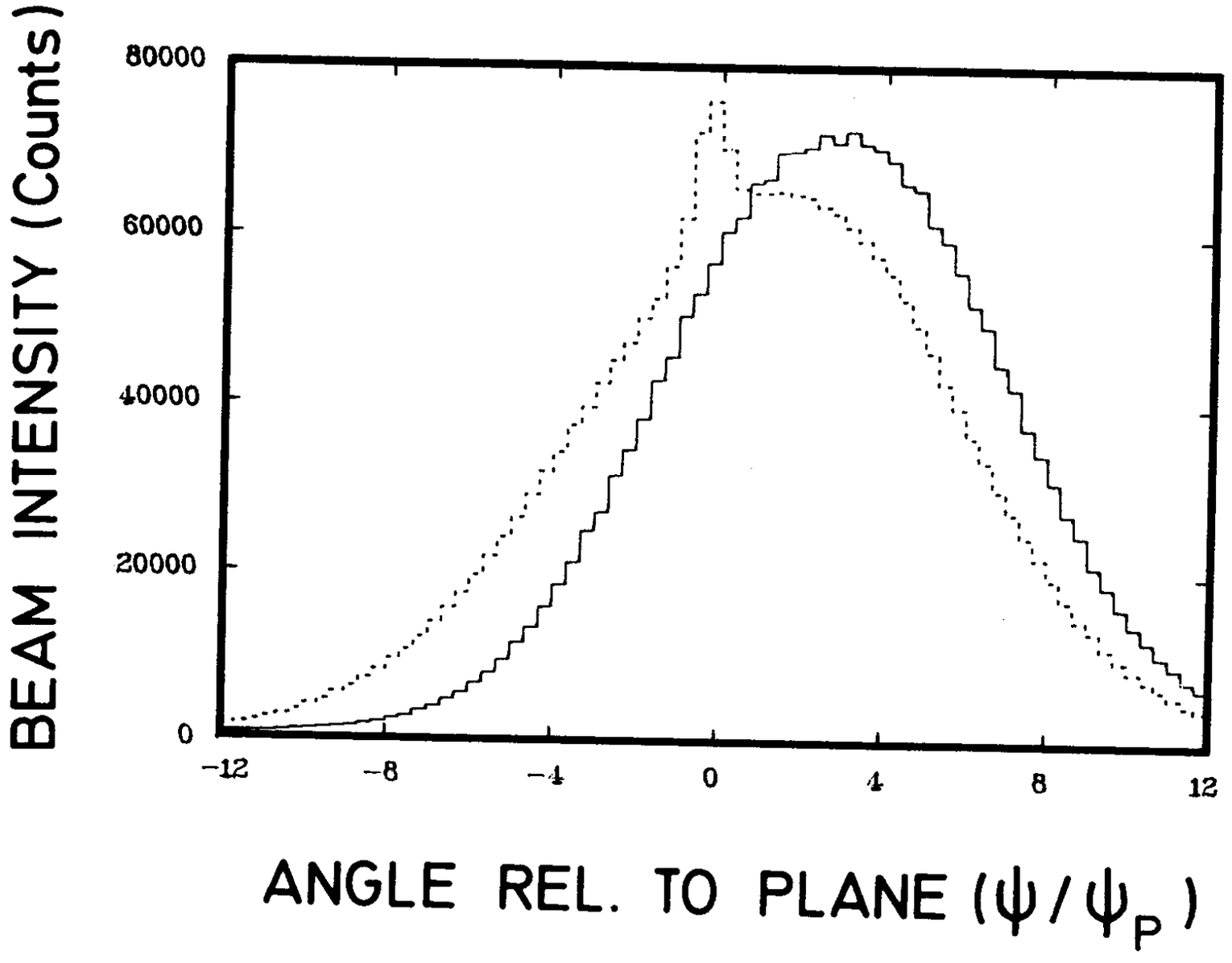
BEAM INTENSITY (Counts)
80000
60000
40000
20000
0
-12
-8
-4
0
4
8
12
ANGLE REL. TO PLANE (ψ/ψP)

Fig. 10

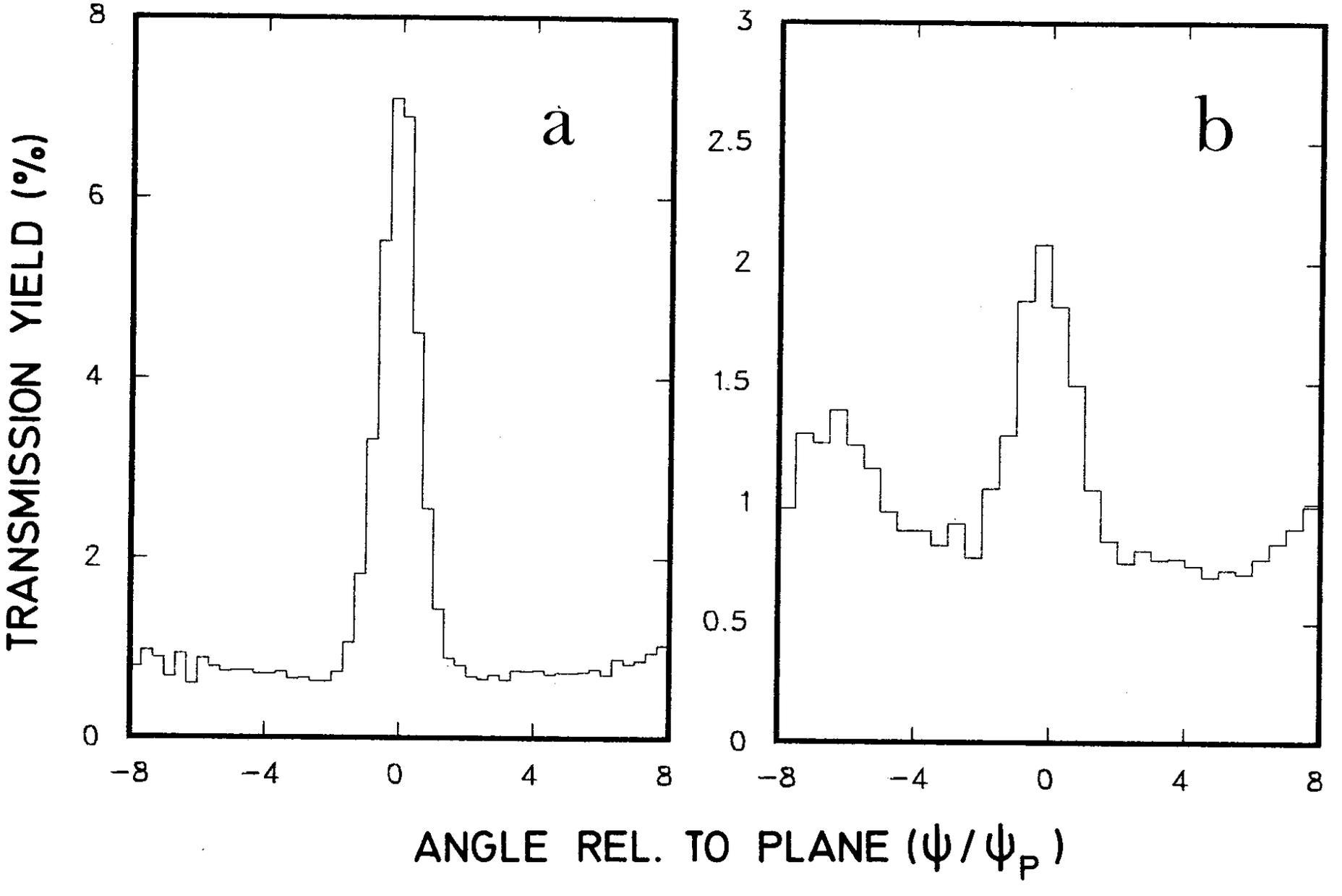
TRANSMISSION YIELD (%)
a
b
8
6
4
2
0
3
2.5
2
1.5
1
0.5
0
−8
−4
0
4
8
ANGLE REL. TO PLANE (ψ/ψP)

Fig. 11

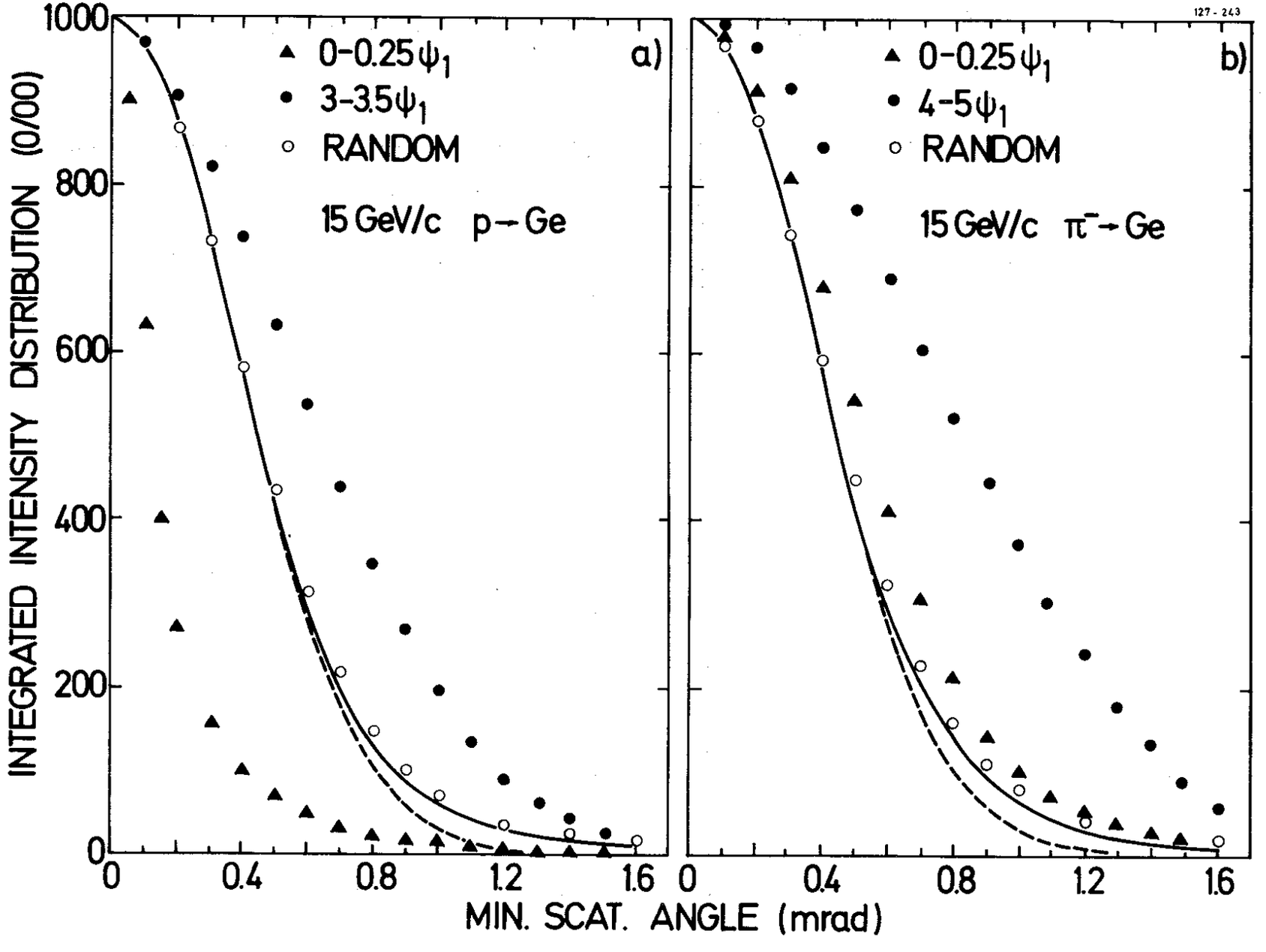
127-243
INTEGRATED INTENSITY DISTRIBUTION (0/00)
1000
800
600
400
200
0
0-0.25ψ1
3-3.5ψ1
RANDOM
15 GeV/c p→Ge
a)
0-0.25ψ1
4-5ψ1
RANDOM
15 GeV/c π⁻→Ge
b)
0
0.4
0.8
1.2
1.6
MIN. SCAT. ANGLE (mrad)

Fig. 12

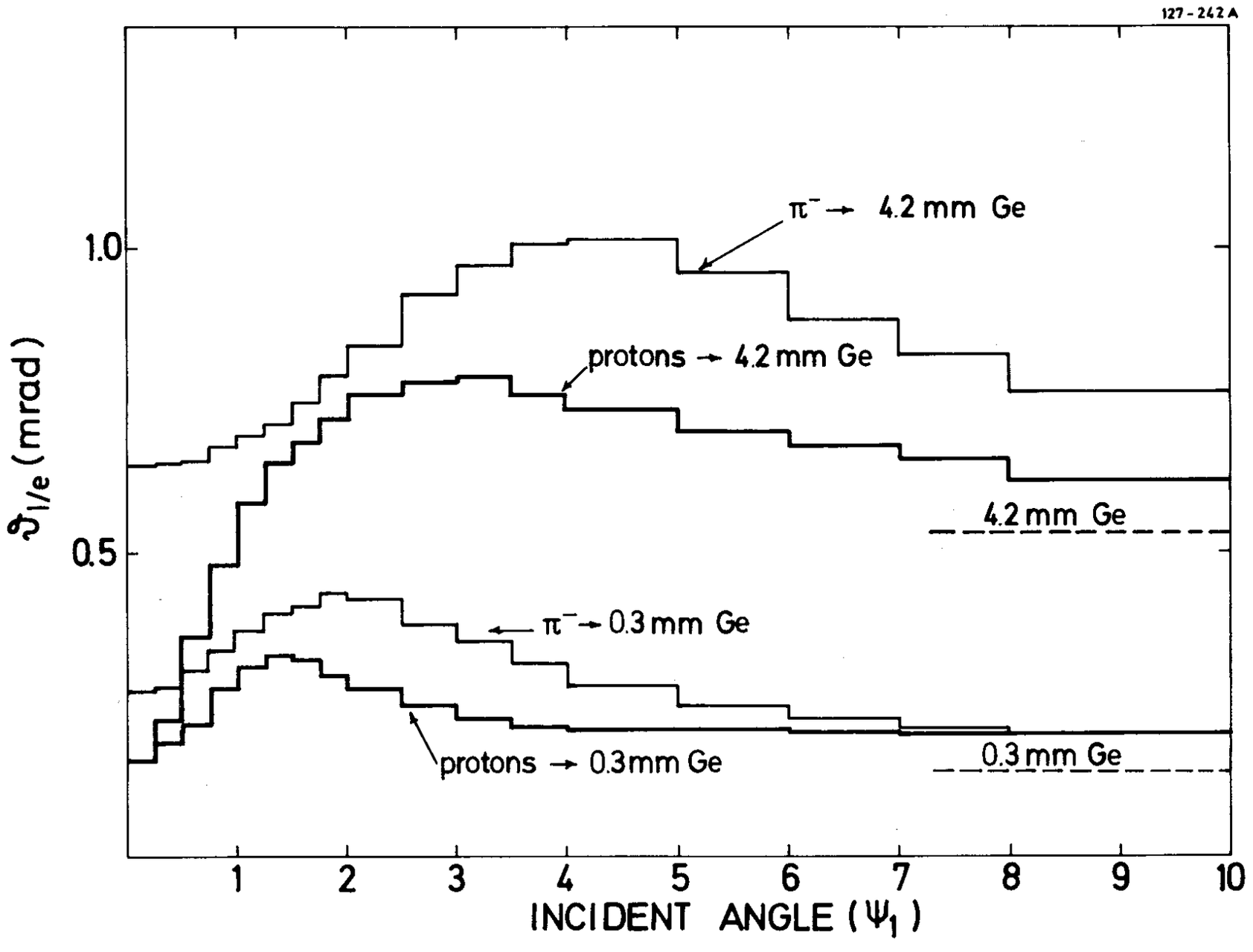
127 - 242 A
1.0
0.5
$\vartheta_{1/e}$ (mrad)
$\pi^- \rightarrow$ 4.2 mm Ge
protons → 4.2 mm Ge
4.2 mm Ge
$\pi^- \rightarrow$ 0.3 mm Ge
protons → 0.3mm Ge
0.3 mm Ge
1
2
3
4
5
6
7
8
9
10
INCIDENT ANGLE (Ψ_1)

Fig.13

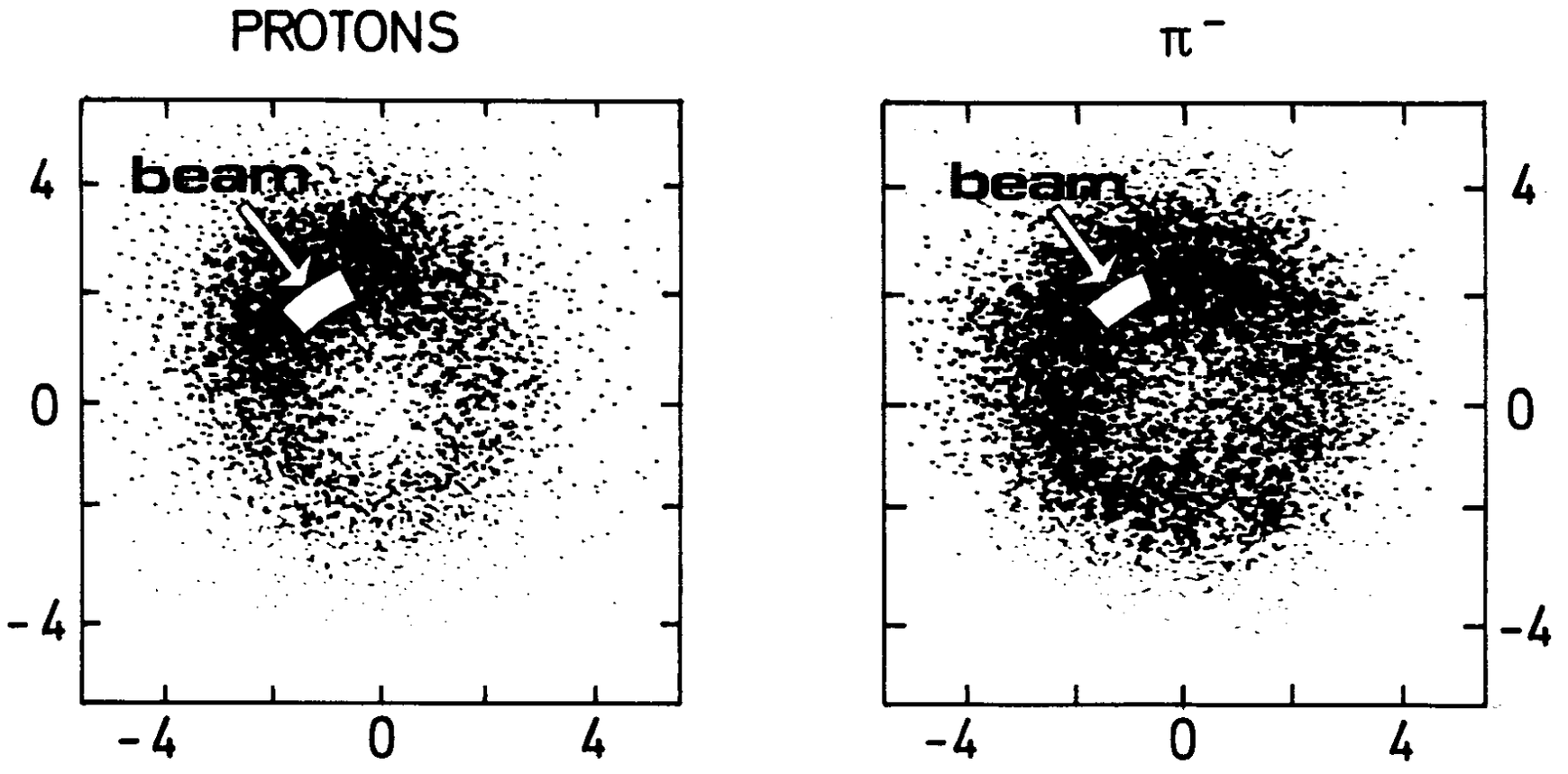
PROTONS
π⁻
beam
beam
4
0
-4
-4
0
4
TRANSMITTED BEAM RELATIVE TO ⟨110⟩ AXIS
ψ / ψ1

Fig.14

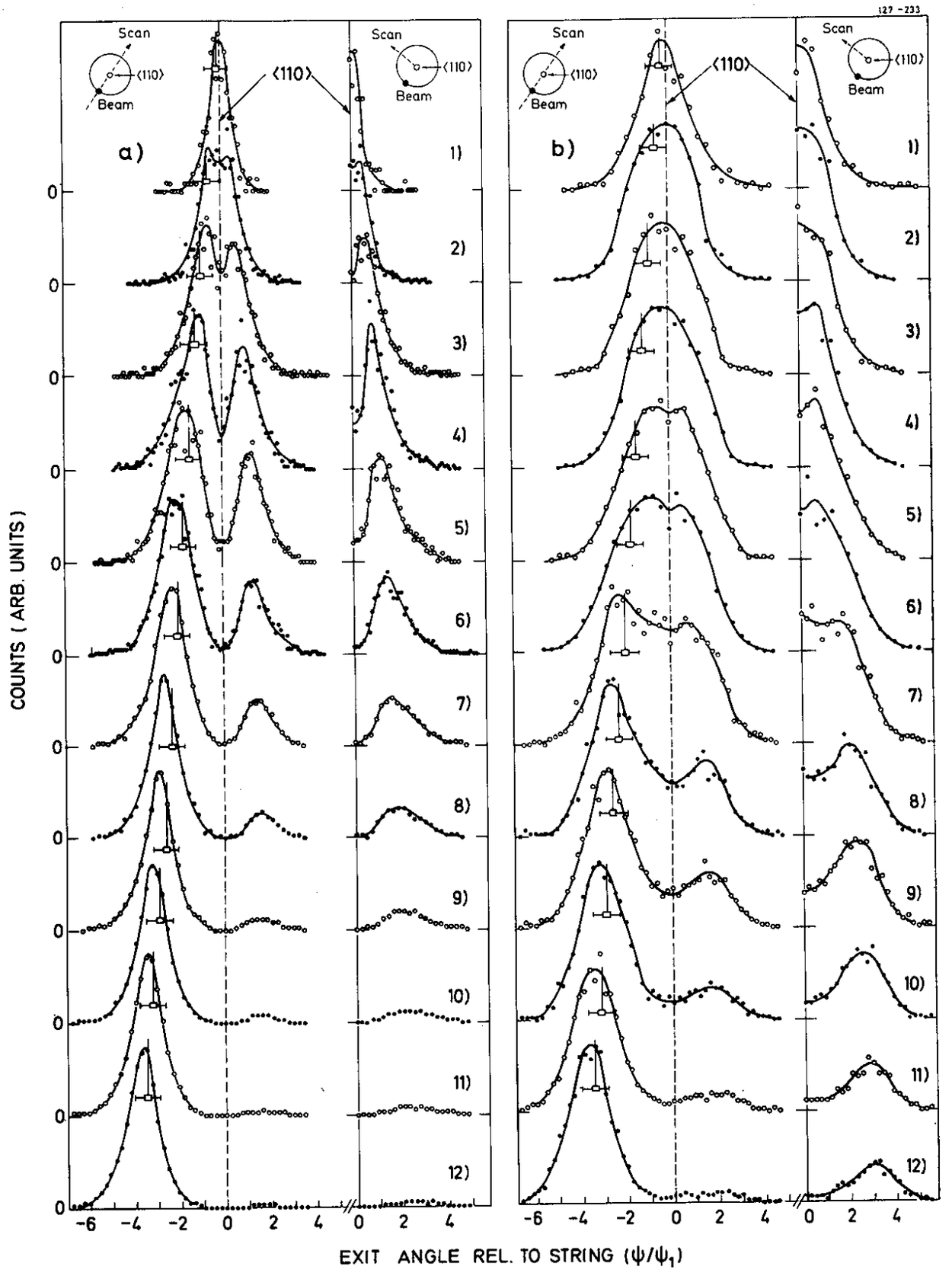
127 -233
Scan
⟨110⟩
Beam
a)
b)
⟨110⟩
1)
2)
3)
4)
5)
6)
7)
8)
9)
10)
11)
12)
0
-6 -4 -2 0 2 4 0 2 4
COUNTS (ARB. UNITS)
EXIT ANGLE REL. TO STRING (ψ/ψ1)

Fig.15

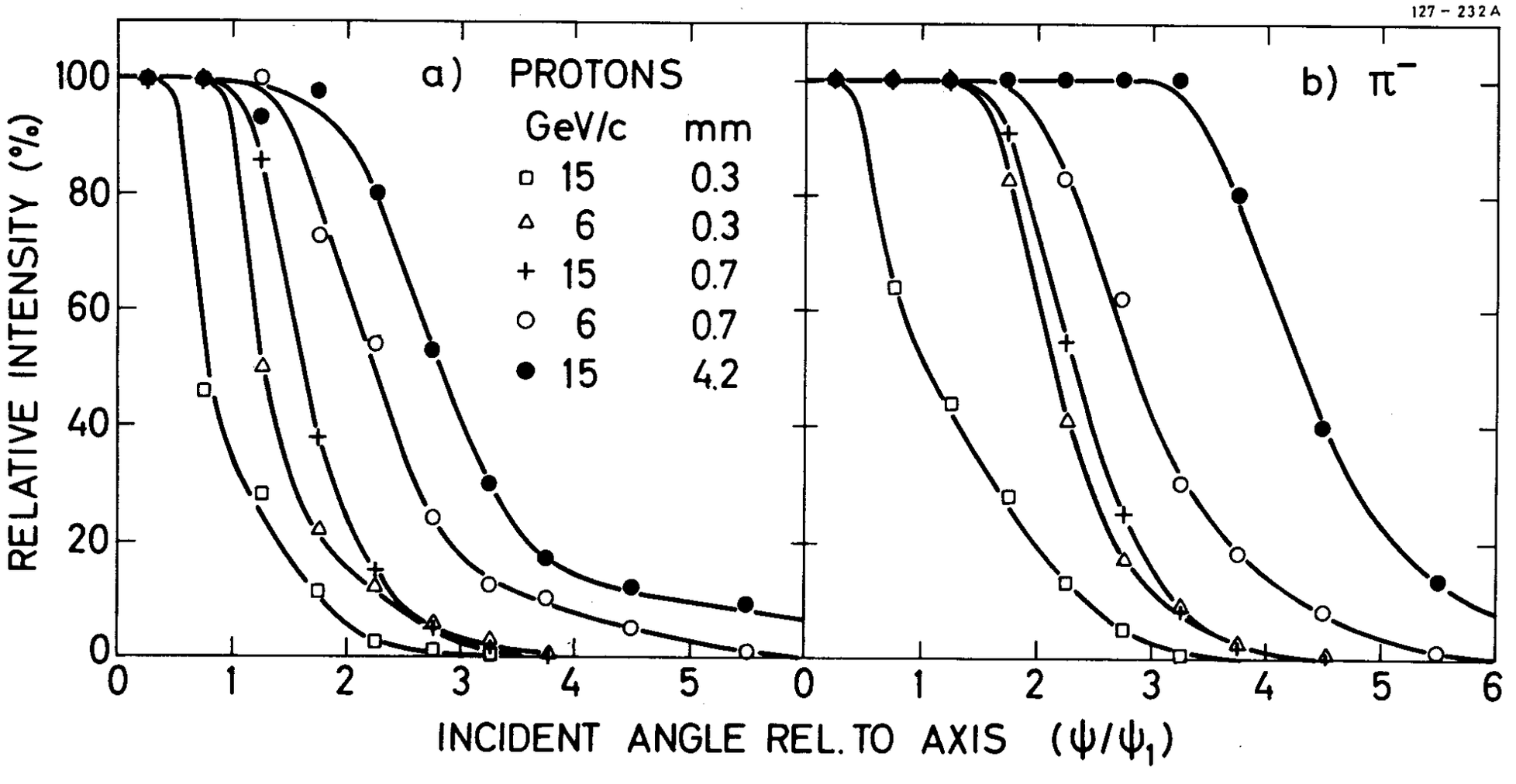
127 - 232A
a) PROTONS
GeV/c mm
15 0.3
6 0.3
15 0.7
6 0.7
15 4.2
b) π⁻
RELATIVE INTENSITY (%)
INCIDENT ANGLE REL. TO AXIS (ψ/ψ1)

Fig.16

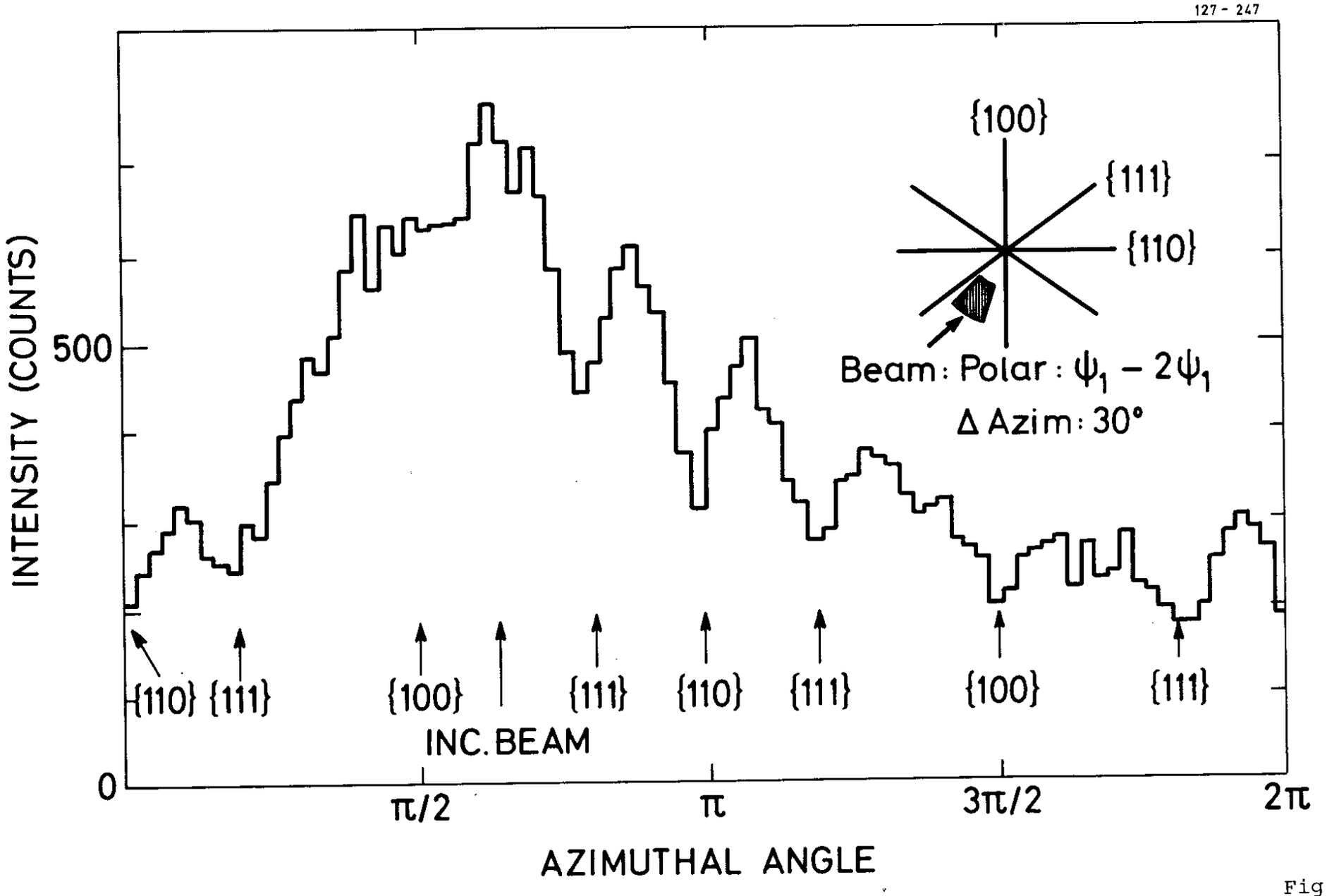
INTENSITY (COUNTS)
500
0
{110}
{111}
{100}
INC. BEAM
{111}
{110}
{111}
{100}
{111}
π/2
π
3π/2
2π
AZIMUTHAL ANGLE
{100}
{111}
{110}
Beam: Polar: $\psi_1 - 2\psi_1$
Δ Azim: 30°

Fig.17

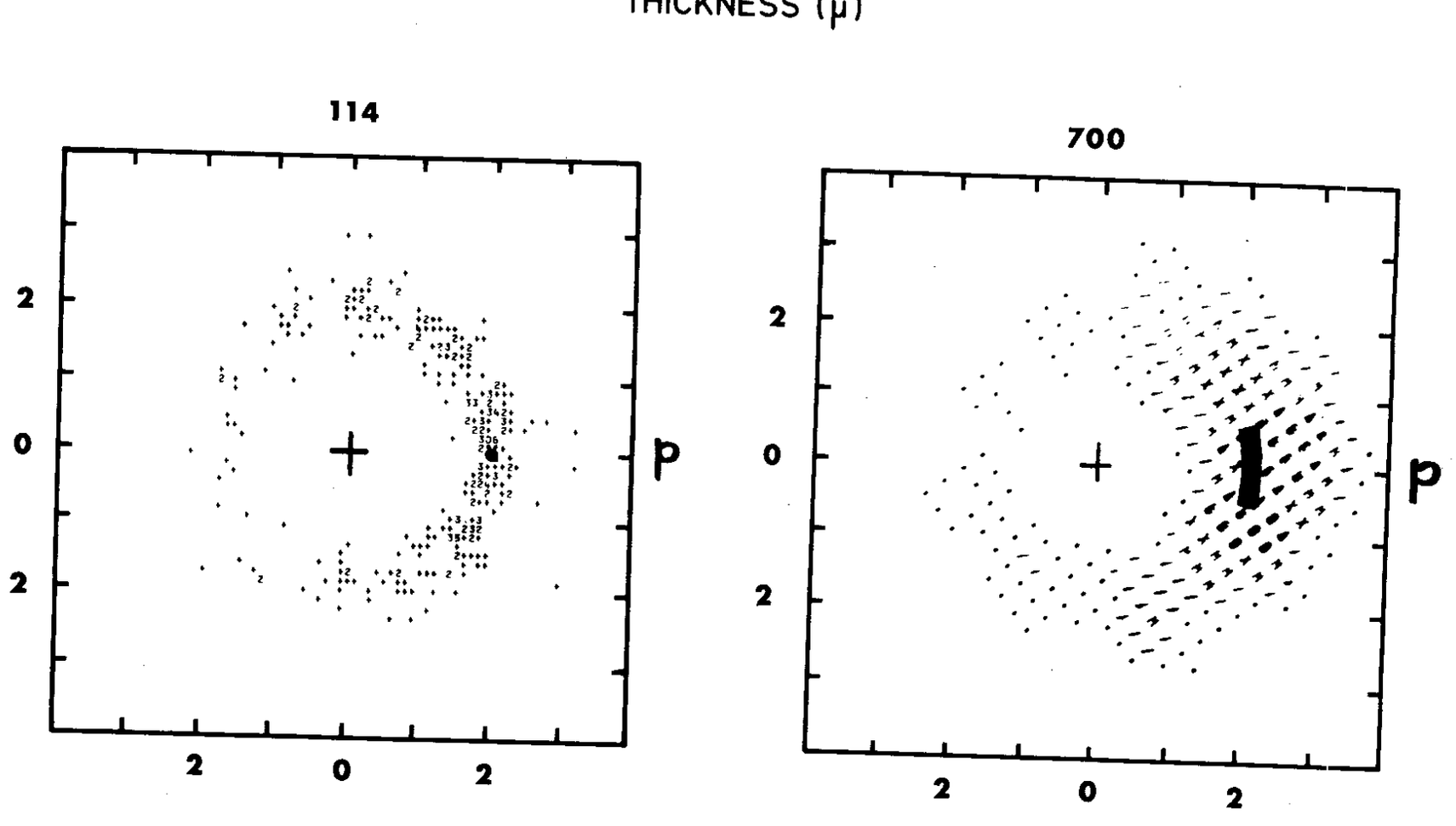
THICKNESS (μ)
114
700
2
0
2
2
0
2
P
2
0
2
2
0
2
P
EXIT ANGLE REL. TO ⟨110⟩ AXIS (ψ/ψ1)

Fig.18

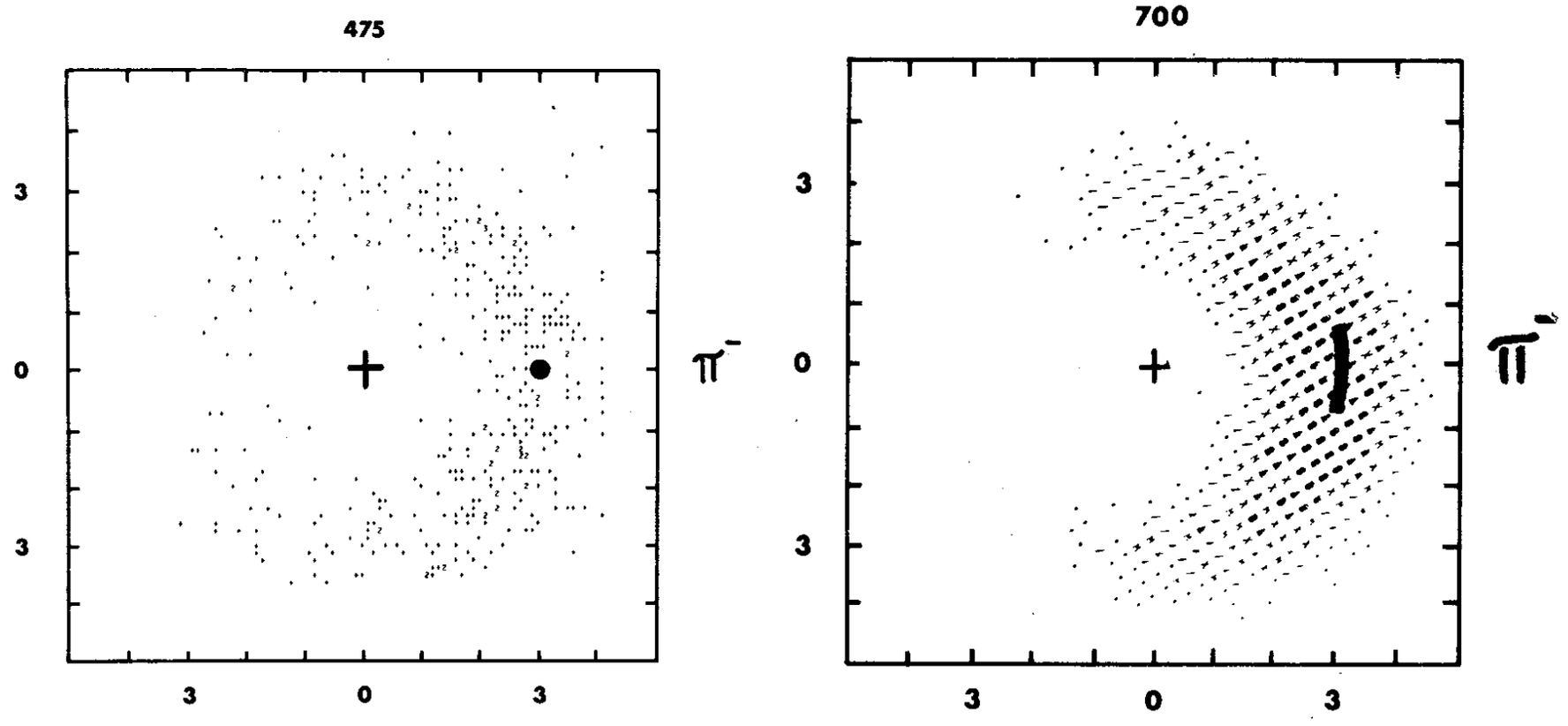

Fig. 19

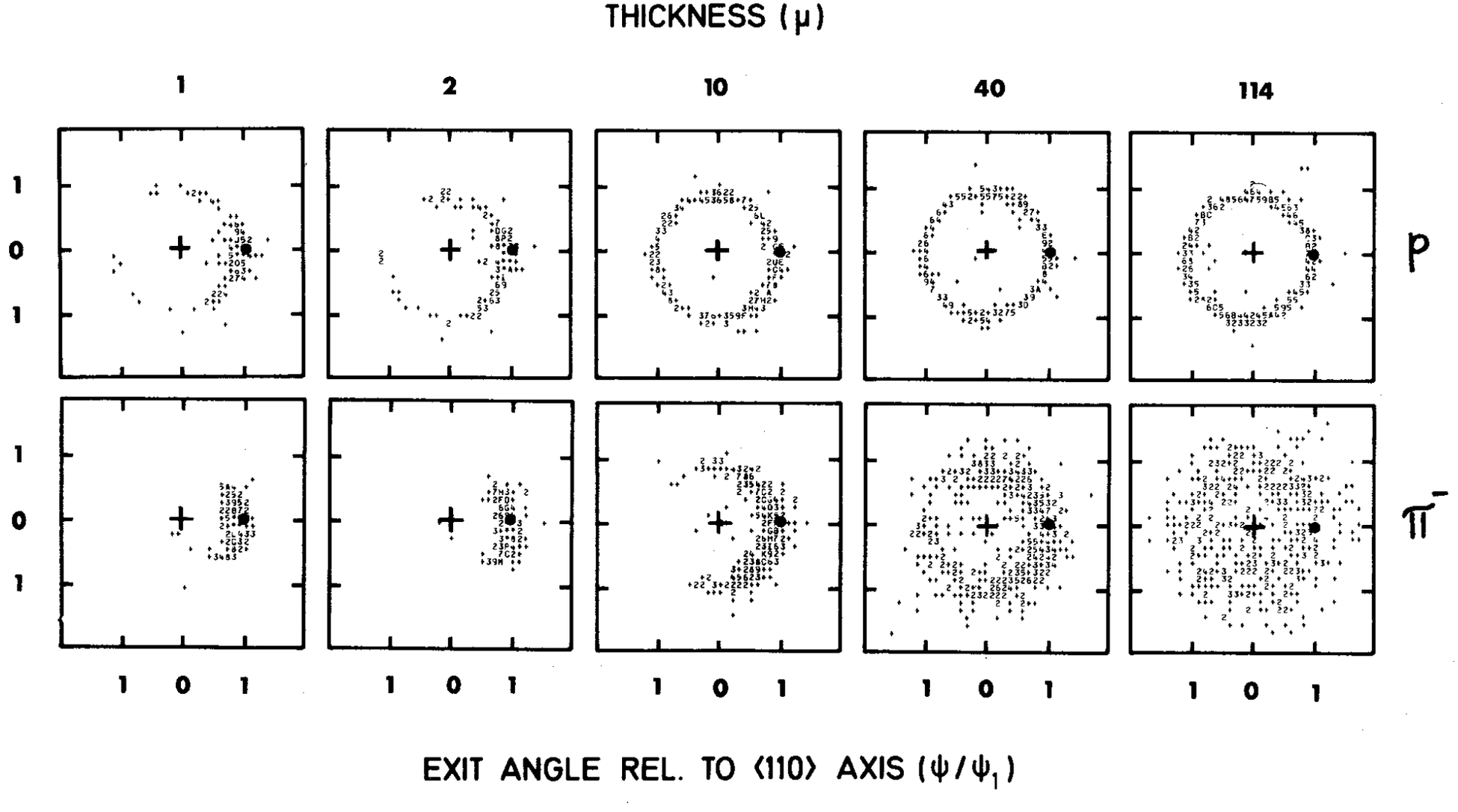

Fig. 20 a

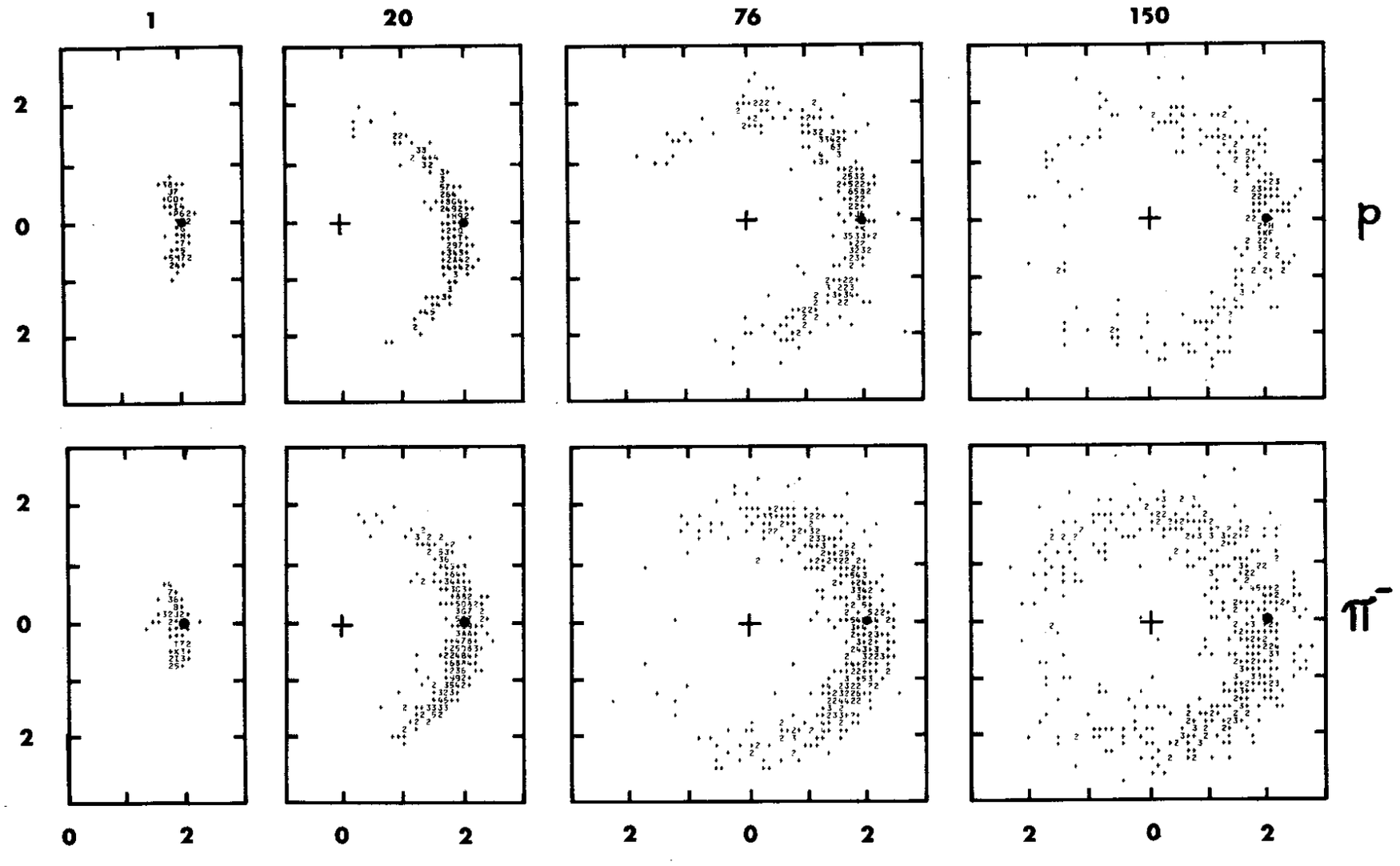

Fig. 20 b

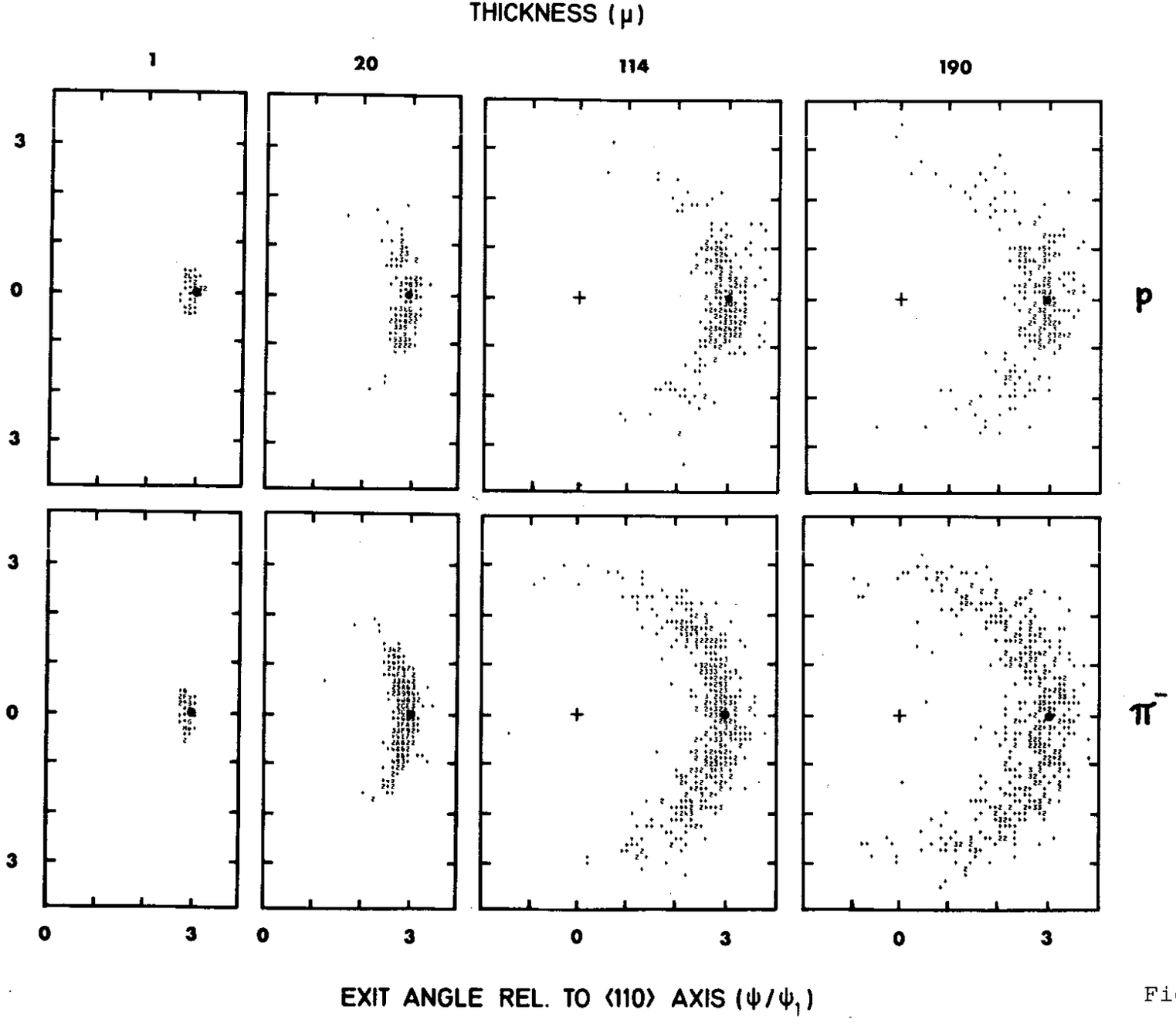
THICKNESS (μ)
1
20
114
190
3
0
3
p
π⁻
0
3
EXIT ANGLE REL. TO ⟨110⟩ AXIS (ψ/ψ1)

Fig. 20 c

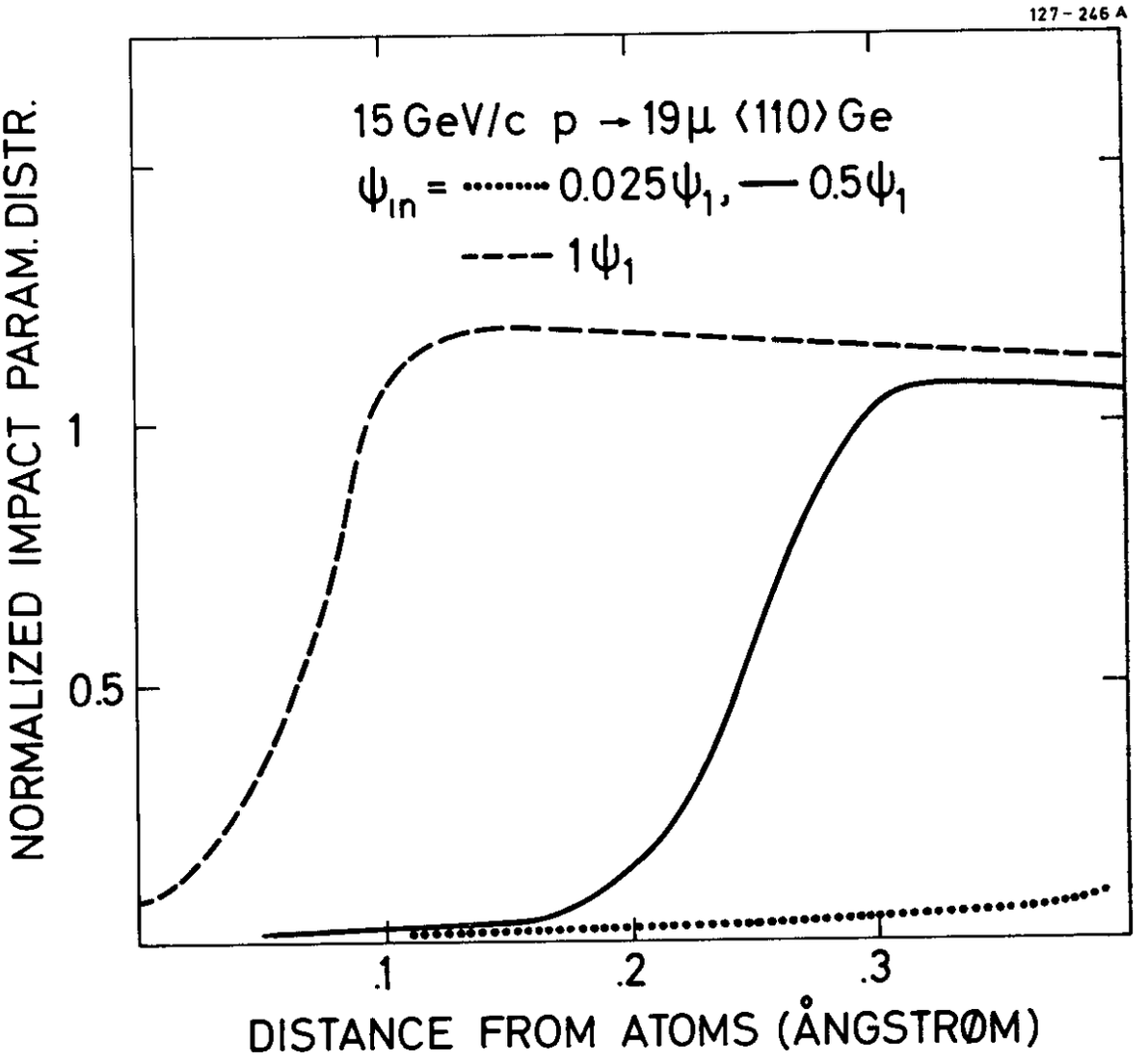
127-246 A
15 GeV/c p → 19μ ⟨110⟩ Ge
ψin = ····· 0.025ψ1, — 0.5ψ1
---- 1ψ1
NORMALIZED IMPACT PARAM. DISTR.
1
0.5
.1
.2
.3
DISTANCE FROM ATOMS (ÅNGSTRØM)

Fig.21

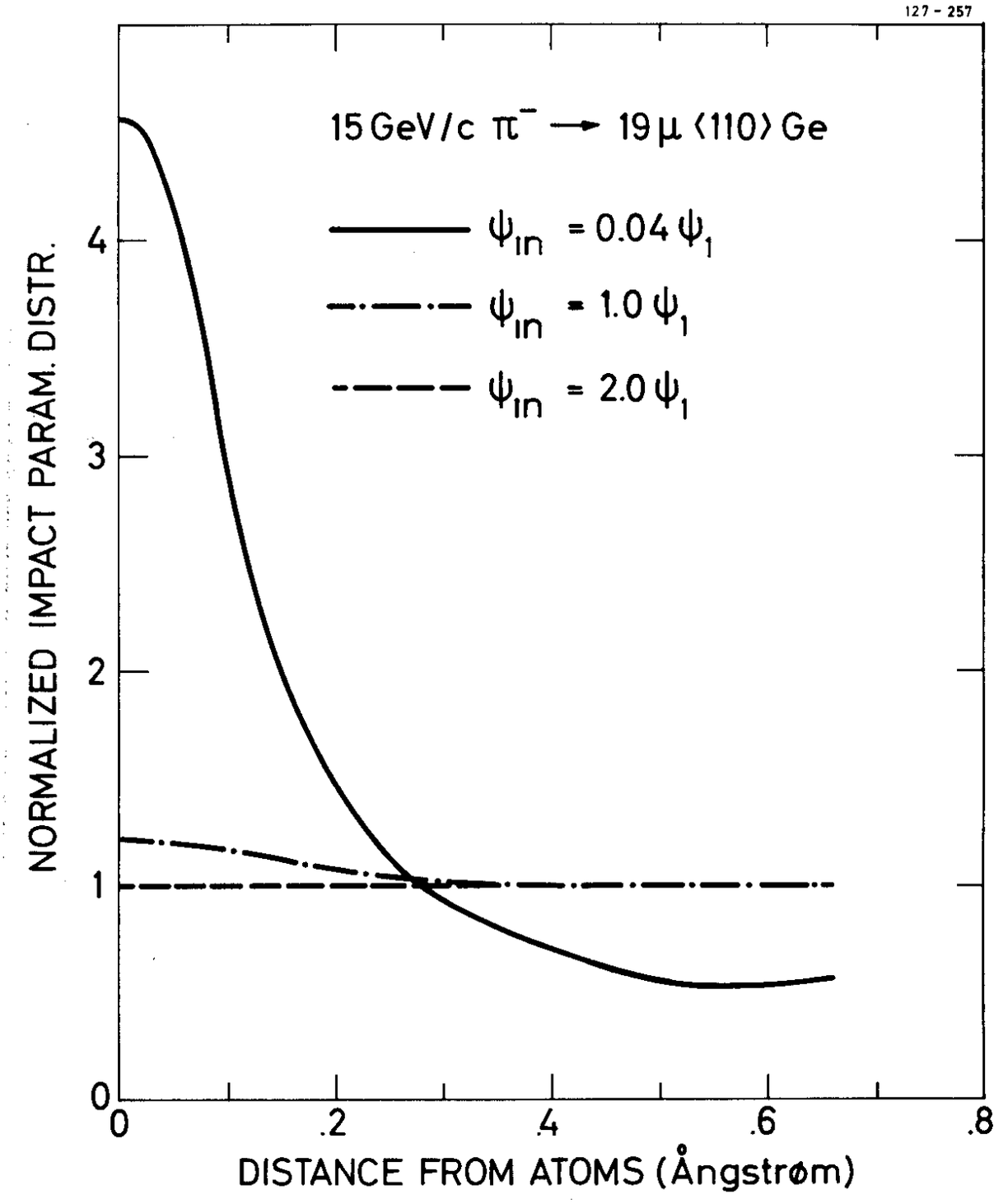
127 - 257
15 GeV/c π⁻ → 19 μ ⟨110⟩ Ge
ψin = 0.04 ψ1
ψin = 1.0 ψ1
ψin = 2.0 ψ1
NORMALIZED IMPACT PARAM. DISTR.
0
1
2
3
4
0
.2
.4
.6
.8
DISTANCE FROM ATOMS (Ångstrøm)

Fig. 22

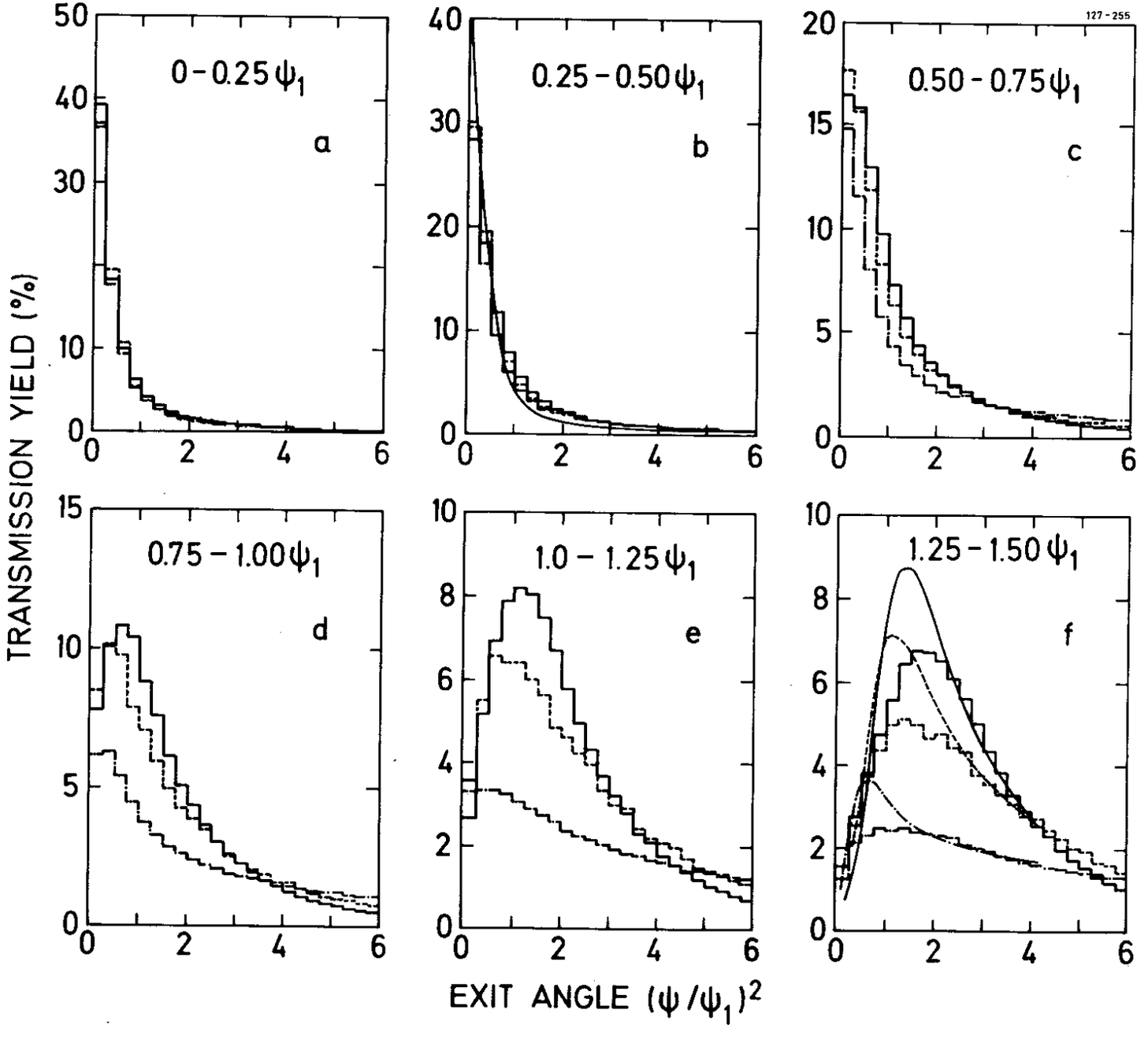
127-255
0-0.25 ψ1
a
0.25-0.50 ψ1
b
0.50-0.75 ψ1
c
0.75-1.00 ψ1
d
1.0-1.25 ψ1
e
1.25-1.50 ψ1
f
TRANSMISSION YIELD (%)
EXIT ANGLE (ψ/ψ1)2

Fig.23

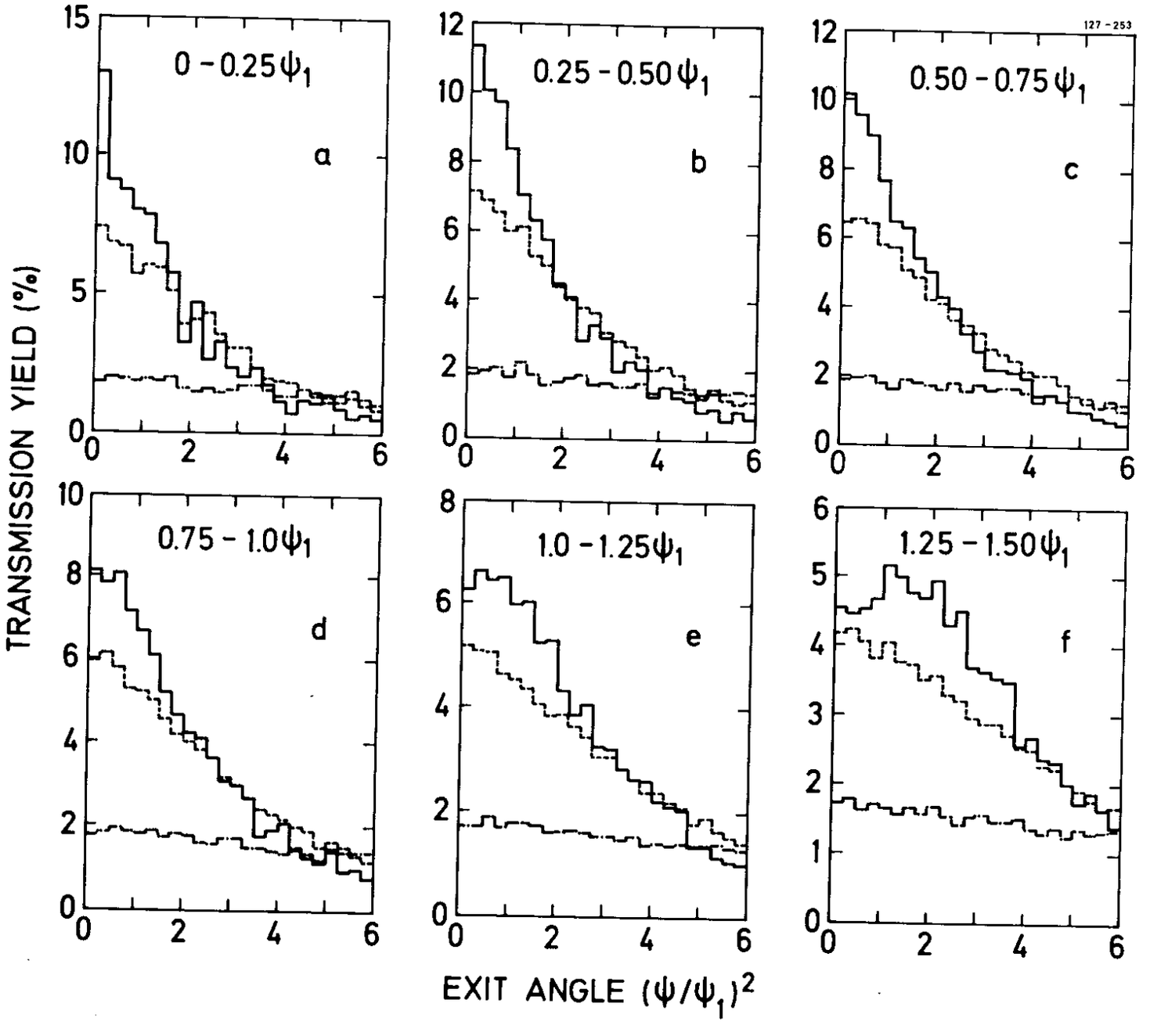
127 - 253
TRANSMISSION YIELD (%)
EXIT ANGLE $(\psi/\psi_1)^2$
0 - 0.25 ψ_1
a
0.25 - 0.50 ψ_1
b
0.50 - 0.75 ψ_1
c
0.75 - 1.0 ψ_1
d
1.0 - 1.25 ψ_1
e
1.25 - 1.50 ψ_1
f

Fig.24

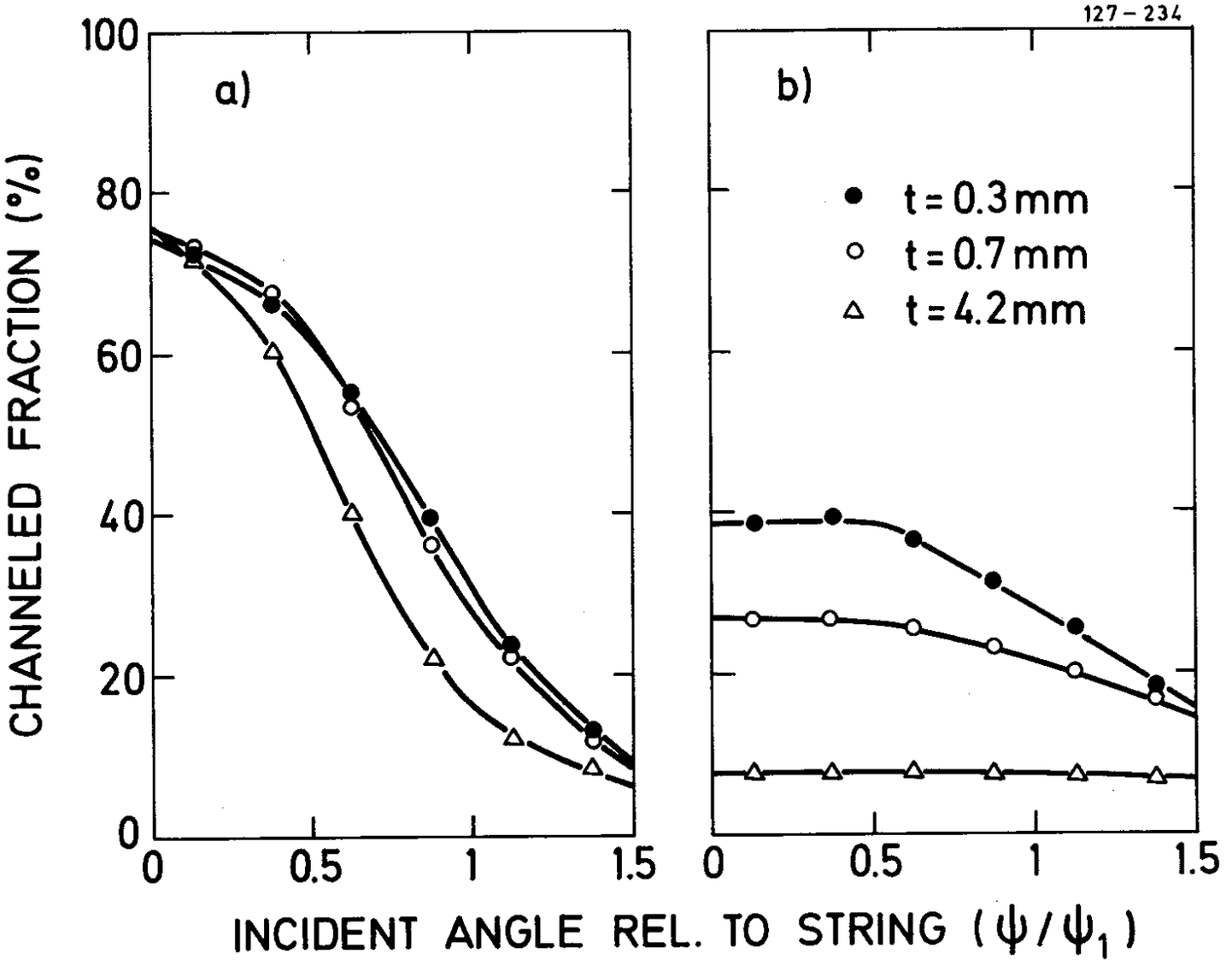
127 – 234
a)
b)
t = 0.3 mm
t = 0.7 mm
t = 4.2 mm
CHANNELED FRACTION (%)
100
80
60
40
20
0
0
0.5
1
1.5
INCIDENT ANGLE REL. TO STRING (ψ / ψ1)

Fig.25

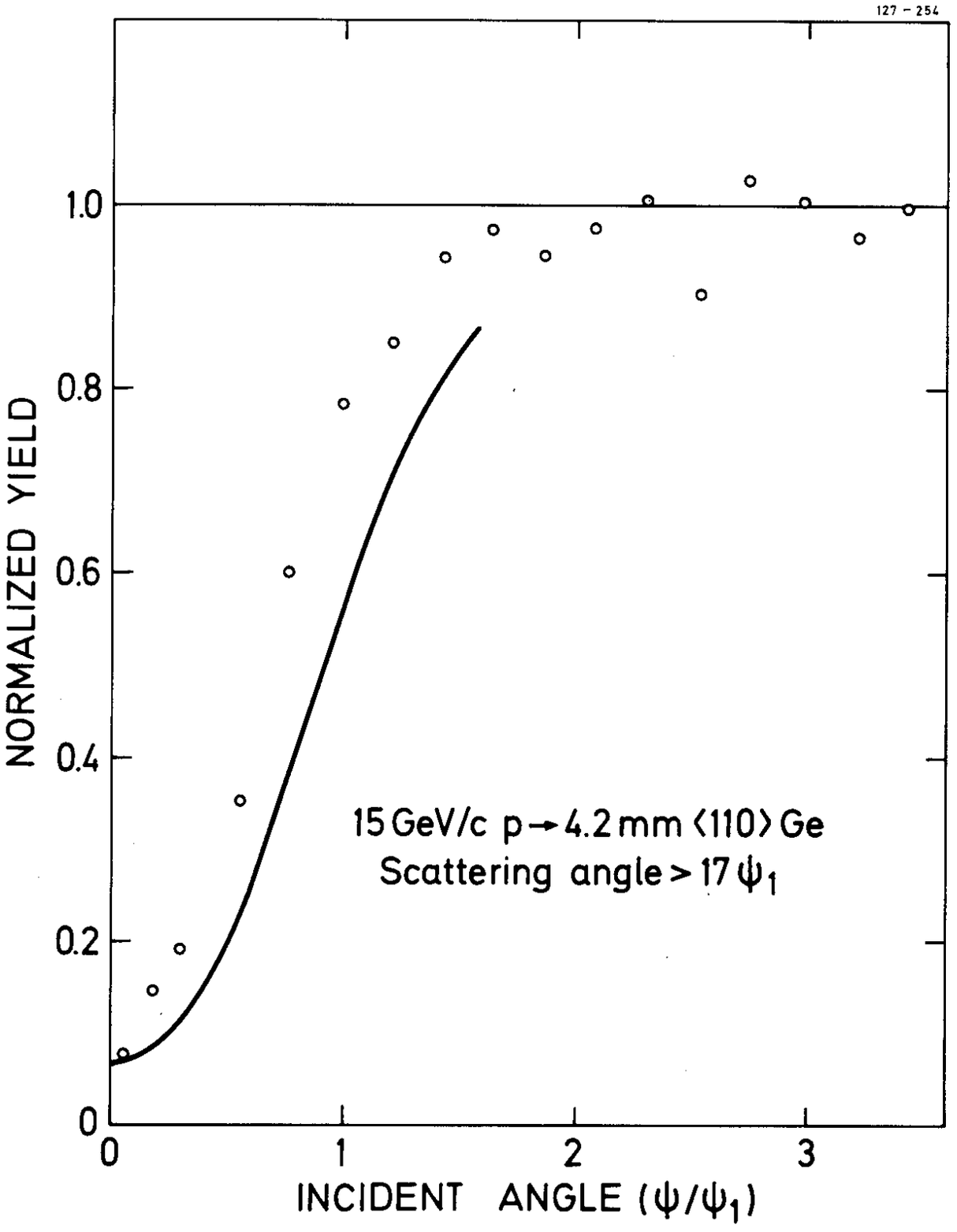
127 - 254
NORMALIZED YIELD
1.0
0.8
0.6
0.4
0.2
0
0
1
2
3
INCIDENT ANGLE (ψ/ψ1)
15 GeV/c p → 4.2 mm ⟨110⟩ Ge
Scattering angle > 17 ψ1

Fig.26

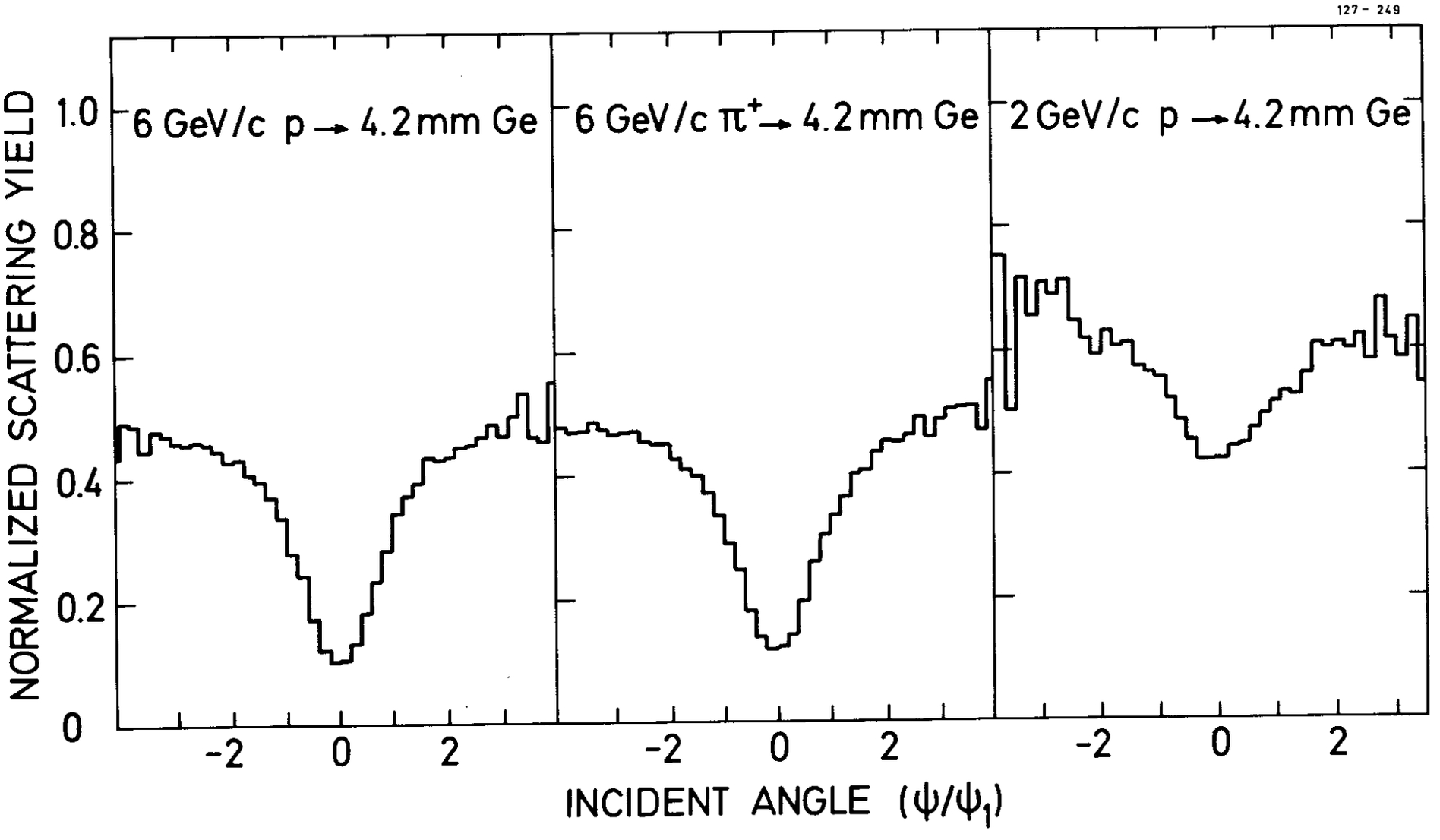
127 - 249
6 GeV/c p → 4.2mm Ge
6 GeV/c π+ → 4.2mm Ge
2 GeV/c p → 4.2mm Ge
NORMALIZED SCATTERING YIELD
1.0
0.8
0.6
0.4
0.2
0
-2
0
2
INCIDENT ANGLE (ψ/ψ1)

Fig.27

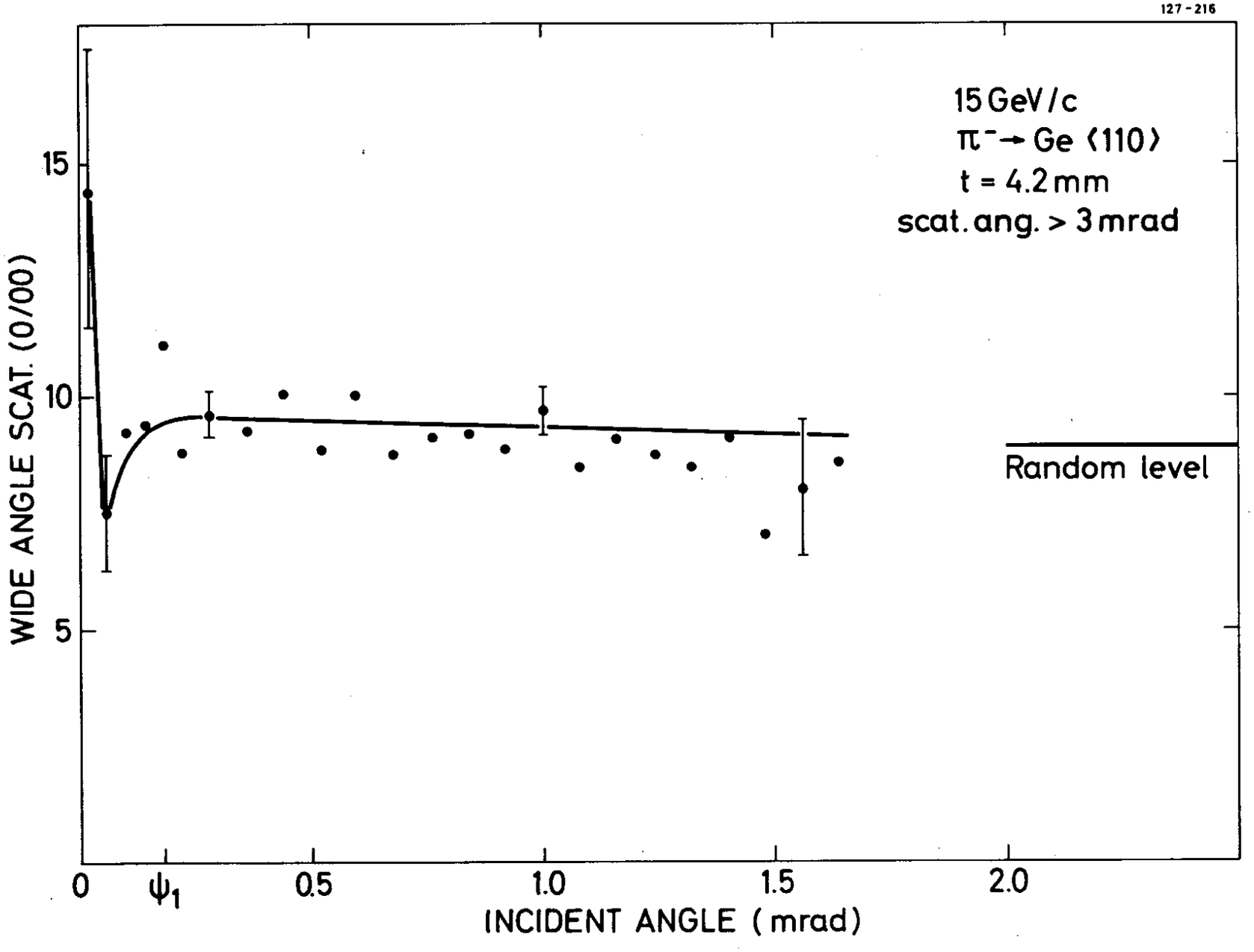
127-216
15 GeV/c
π⁻ → Ge ⟨110⟩
t = 4.2 mm
scat. ang. > 3 mrad
Random level
WIDE ANGLE SCAT. (0/00)
15
10
5
0
ψ1
0.5
1.0
1.5
2.0
INCIDENT ANGLE (mrad)

Fig.28

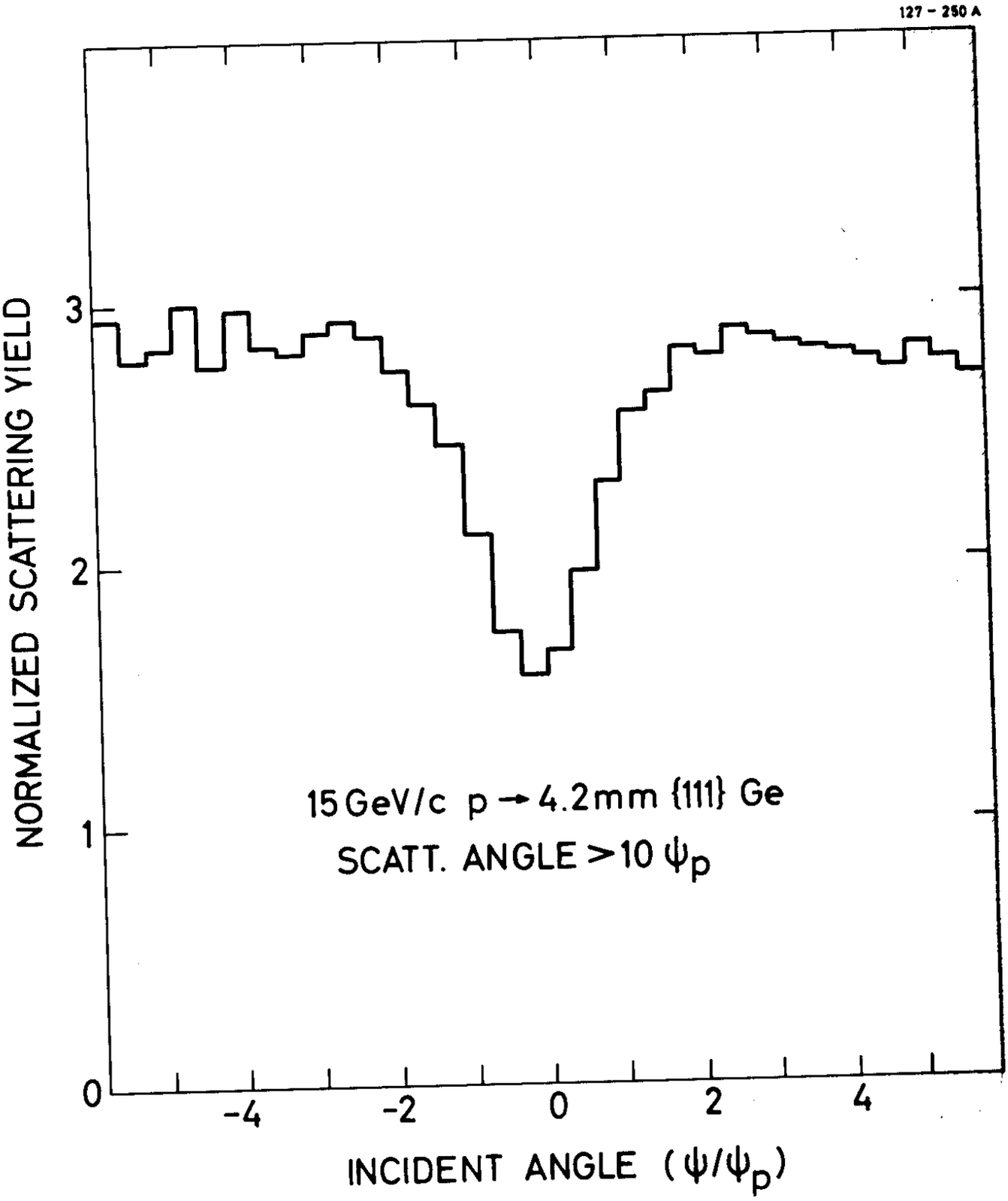
127 - 250 A
NORMALIZED SCATTERING YIELD
3
2
1
0
-4
-2
0
2
4
15 GeV/c p → 4.2mm {111} Ge
SCATT. ANGLE > 10 ψp
INCIDENT ANGLE (ψ/ψp)

Fig.29

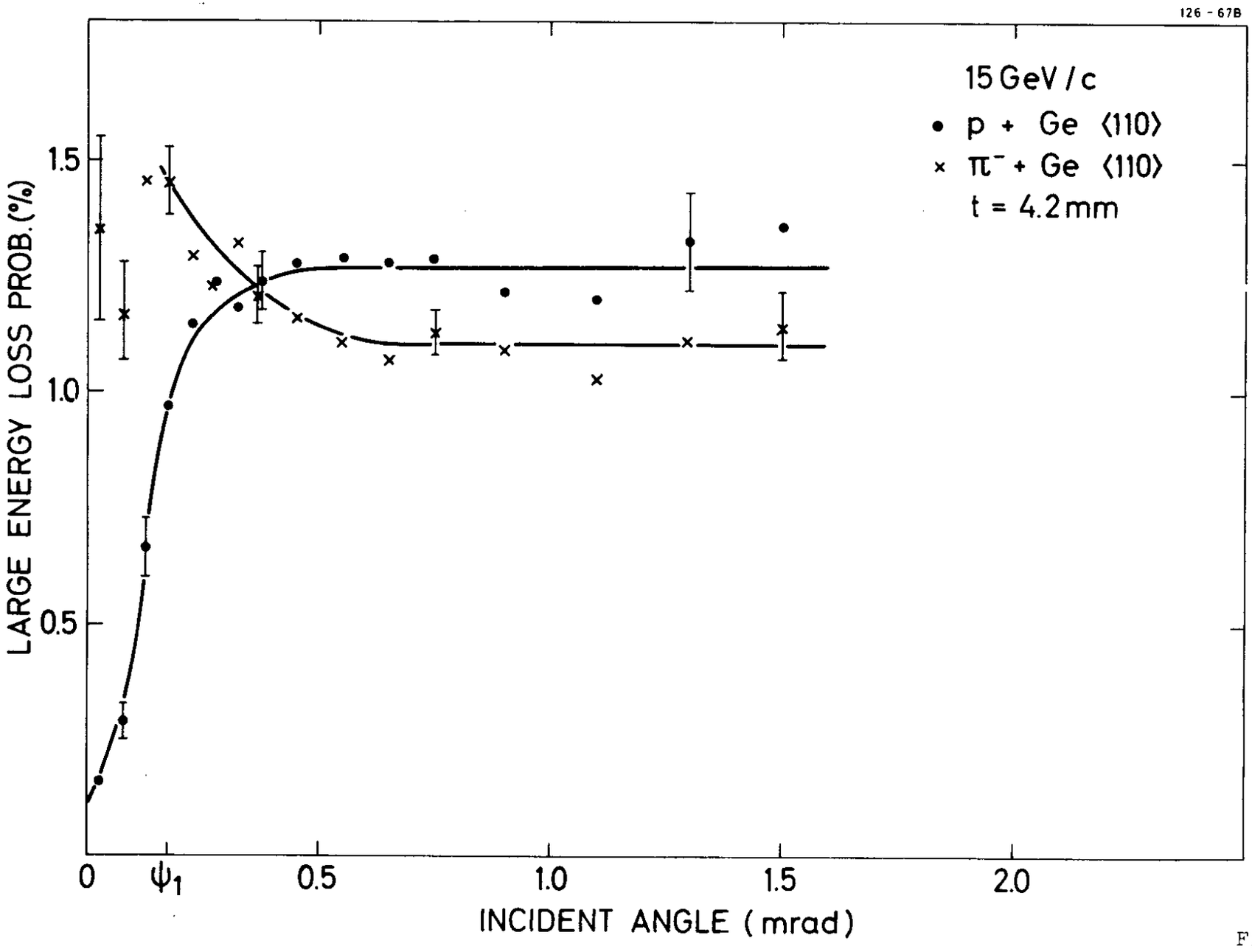
126 - 67B
15 GeV / c
• p + Ge ⟨110⟩
× π⁻ + Ge ⟨110⟩
t = 4.2 mm
LARGE ENERGY LOSS PROB. (%)
1.5
1.0
0.5
0
ψ1
0.5
1.0
1.5
2.0
INCIDENT ANGLE (mrad)

Fig.30

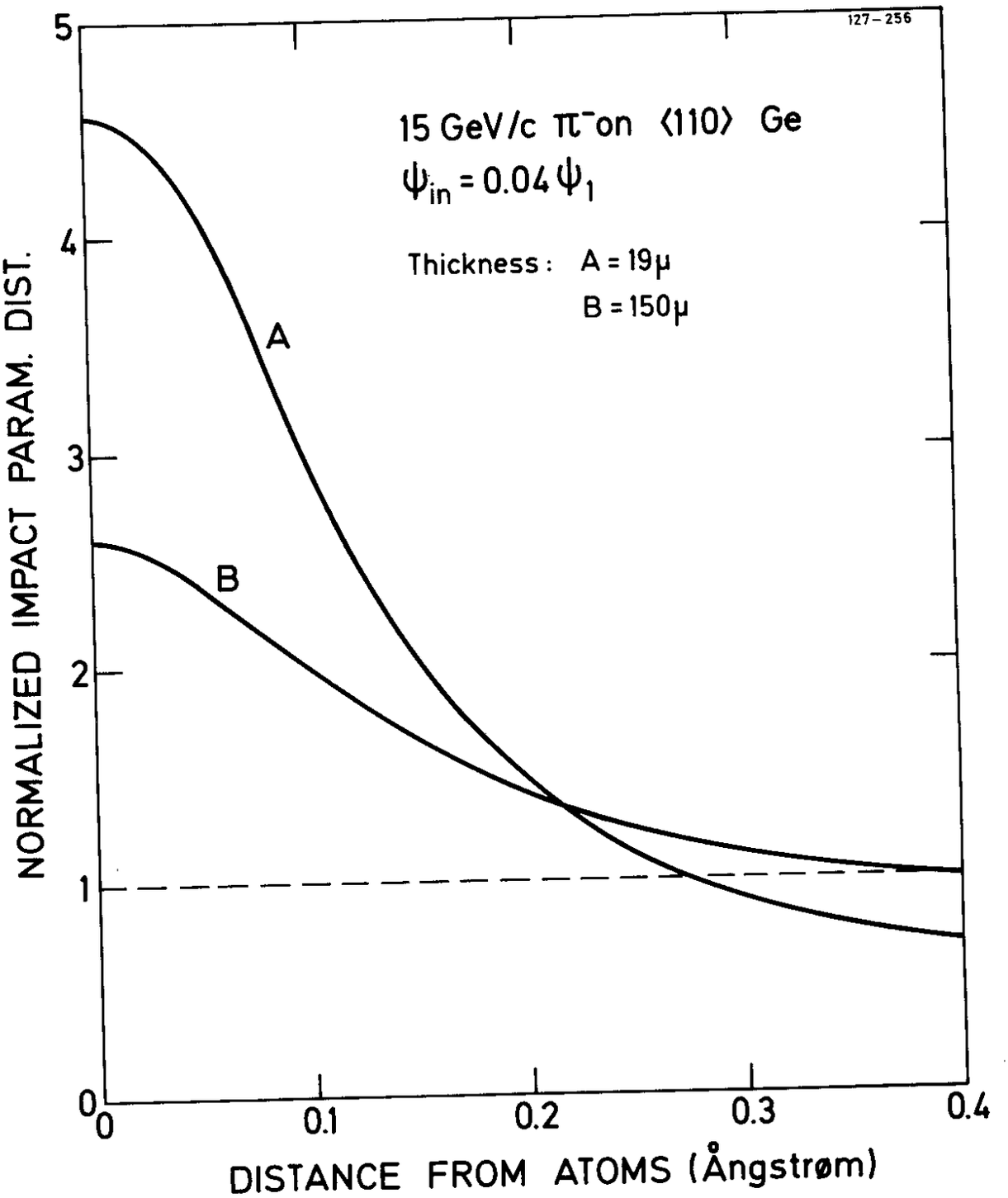
127-256
15 GeV/c π⁻on ⟨110⟩ Ge
$\psi_{in} = 0.04\,\psi_1$
Thickness : A = 19μ
B = 150μ
A
B
NORMALIZED IMPACT PARAM. DIST.
DISTANCE FROM ATOMS (Ångstrøm)
0
1
2
3
4
5
0
0.1
0.2
0.3
0.4

Fig.31

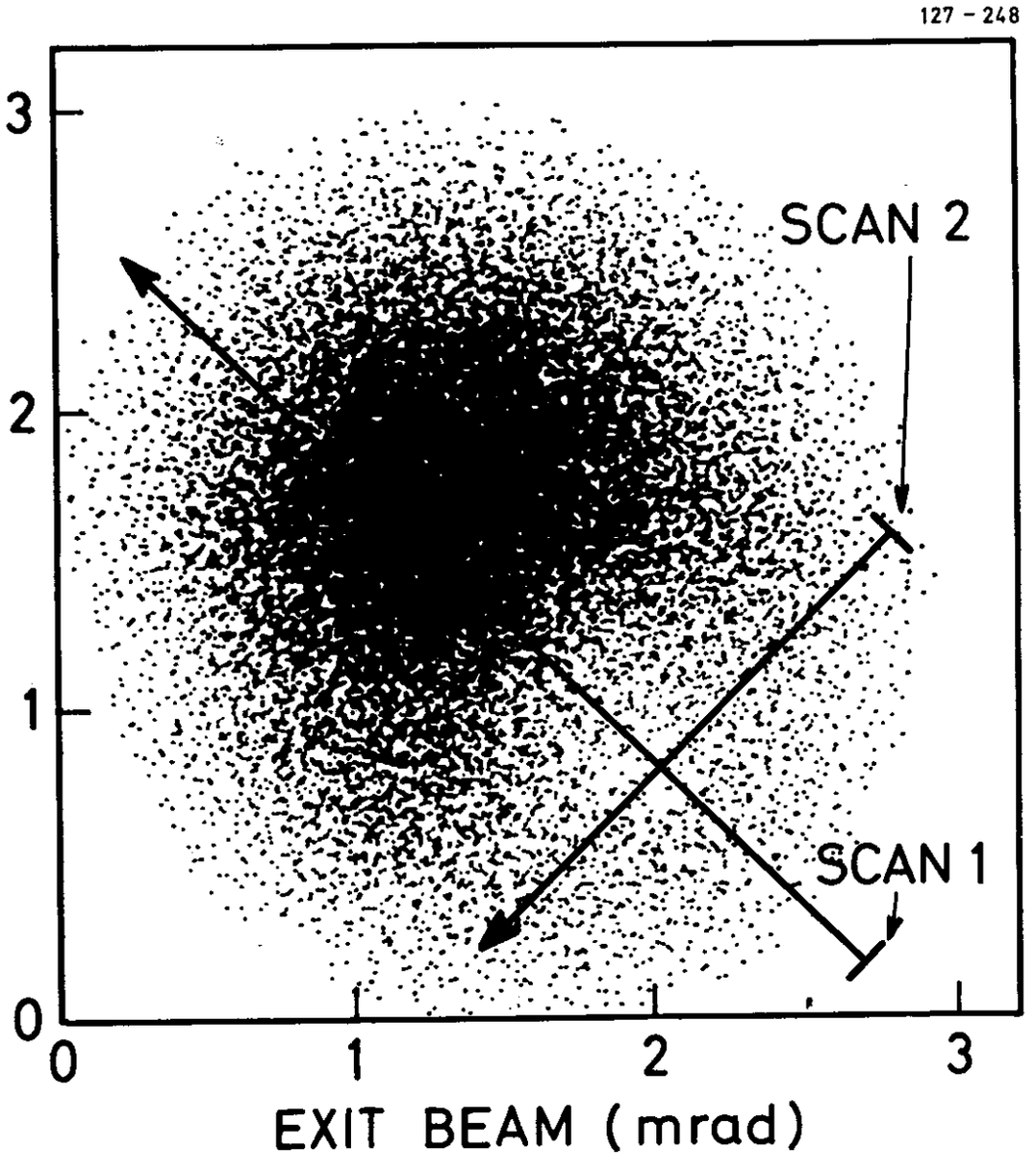

Fig.32

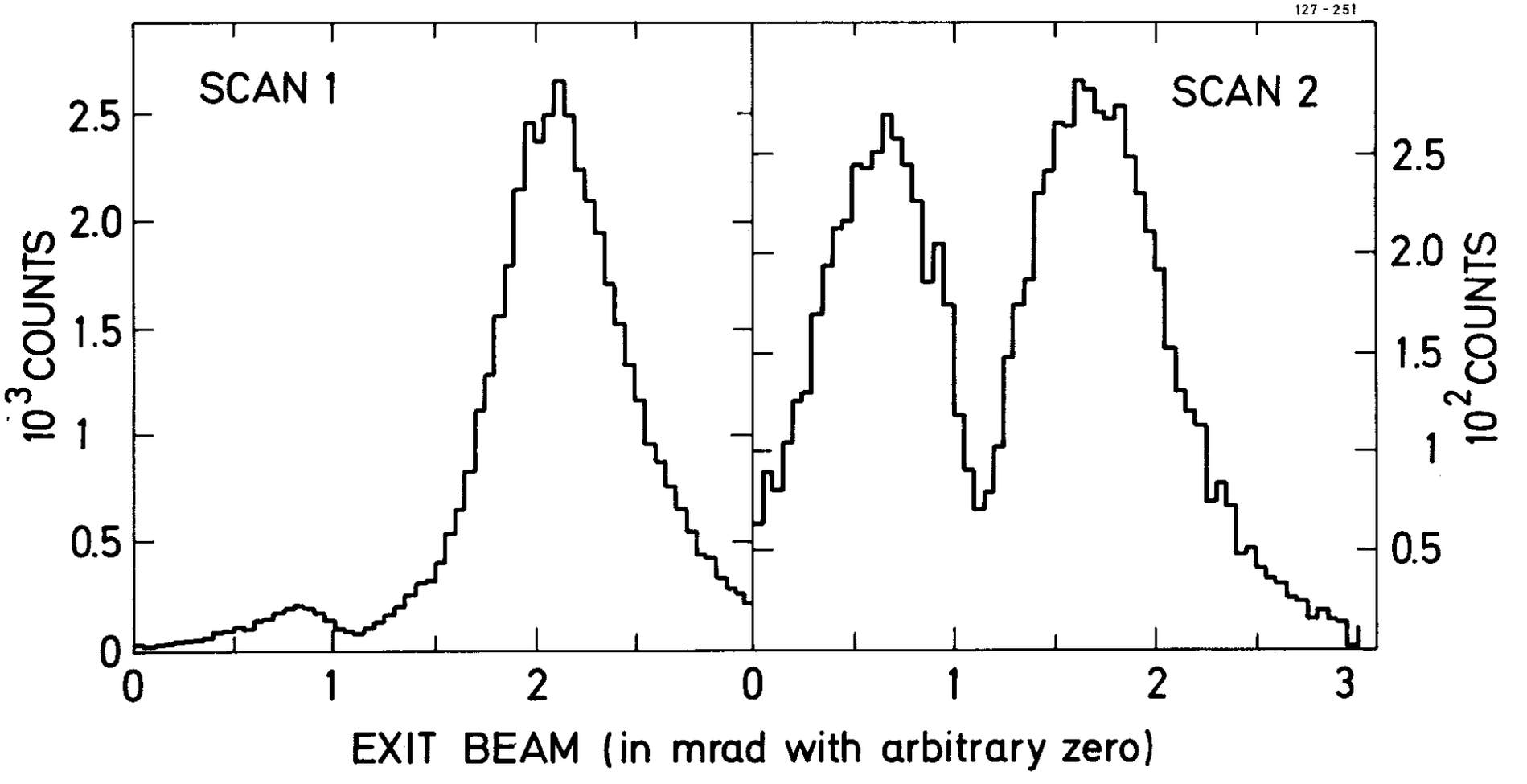
127 - 251
SCAN 1
SCAN 2
10^3 COUNTS
10^2 COUNTS
0
0.5
1
1.5
2
2.5
3
EXIT BEAM (in mrad with arbitrary zero)

Fig.33

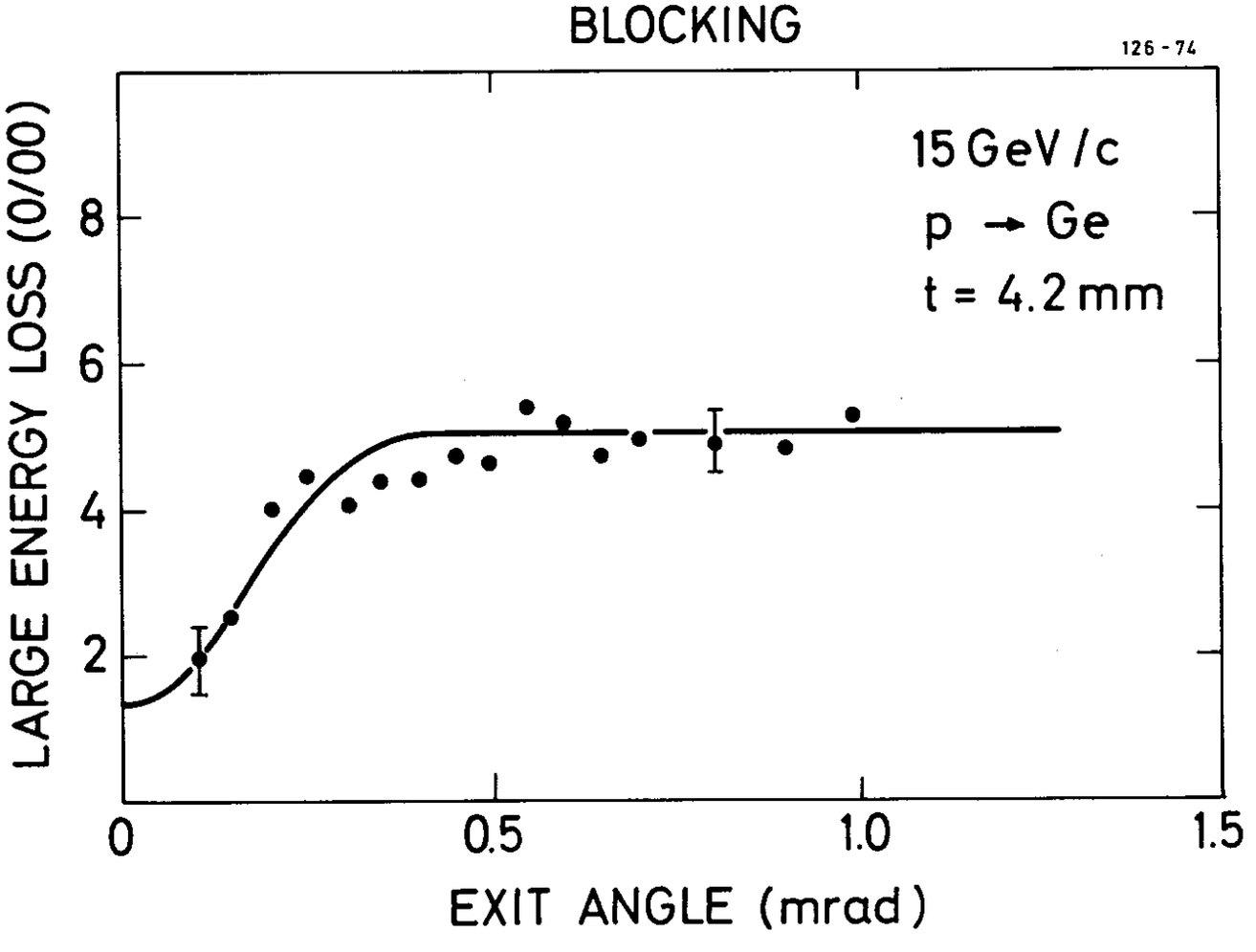
BLOCKING
126 - 74
15 GeV/c
p → Ge
t = 4.2 mm
LARGE ENERGY LOSS (0/00)
8
6
4
2
0
0.5
1.0
1.5
EXIT ANGLE (mrad)

Fig.34